DESIGN AND PERFORMANCE OF HIGH LASER POWER INTERFEROMETERS FOR
GRAVITATIONAL-WAVE DETECTION

By

KATHERINE LAIRD DOOLEY

A DISSERTATION PRESENTED TO THE GRADUATE SCHOOL
OF THE UNIVERSITY OF FLORIDA IN PARTIAL FULFILLMENT
OF THE REQUIREMENTS FOR THE DEGREE OF
DOCTOR OF PHILOSOPHY

UNIVERSITY OF FLORIDA

2011

My dedication.

ACKNOWLEDGMENTS

Some personal acknowledgements–professors, fellow grad students, friends, family.

Acknowledgments for the funding of LIGO.

TABLE OF CONTENTS

7

LIST OF FIGURES

9

LIST OF SYMBOLS, NOMENCLATURE, AND ABBREVIATIONS

ADC   analog-to-digital converter

ASC   Angular Sensing and Control

DAC   digital-to-analog converter

EOM   electro-optic modulator

FI   Faraday isolator

GW   gravitational wave

IO   Input Optics

LIGO   Laser Interferometer Gravitational-wave Observatory

LSC   length sensing and control

MC   mode cleaner

MMT   mode matching telescope

PSL   pre-stabilized laser

PRC   power recycling cavity

REFL   reflected beam

RF   radio frequency

RM   recycling mirror

TGG   Terbium Gallium Garnate

TM   test mass

VIRGO   Variability of Solar Irradiance and Gravity Oscillations

WFS   wave-front sensor

Abstract of dissertation Presented to the Graduate School
of the University of Florida in Partial Fulfillment of the
Requirements for the Degree of Doctor of Philosophy

DESIGN AND PERFORMANCE OF HIGH LASER POWER INTERFEROMETERS FOR
GRAVITATIONAL-WAVE DETECTION

By

Katherine Laird Dooley

September 2011

Chair: David Reitze
Major: Physics

A prediction of Einstein's general theory of relativity, gravitational waves are perturbations
of the flat space-time Minkowski metric that travel at the speed of light. Indirectly measured by
Hulse and Taylor in the 1970s through the energy they carried away from a binary pulsar system,
gravitational waves have yet to be directly detected. The Laser Interferometer Gravitational-wave
Observatory (LIGO) is part of a global network of gravitational-wave detectors that seeks to
directly detect gravitational waves and to study their sources.

LIGO operates on the principle of measuring the gravitational wave's physical signature
of a strain, or relative displacement of inertial masses. An extremely small effect whose biggest
of expected transient signals on Earth is on the order of 10^{-23} (verify this!), gravitational-wave
strain can only be measured by detectors so sensitive to displacement as to (collide with) brush
into the realm of quantum physics. To improve their sensitivities and to demonstrate advanced
technologies, the LIGO observatories in Hanford, WA and Livingston, LA underwent an upgrade
between fall 2007 and summer 2009 called Enhanced LIGO. This dissertation focuses on the
experimental challenges of one of the goals of the upgrade: operating at an increased laser power.

Write this final paragraph describing work.

CHAPTER 1
PURPOSE OF THIS WORK

The purpose of this work is to demonstrate the capability of an interferometric gravitational wave detector to operate at several times the highest of laser powers previously used. From a naïve standpoint, more power is desirable since strain sensitivity improves by $\sqrt{P}$ in the high frequency (> 200 Hz) shot-noise-limited region. However, as detectors become more sensitive at low frequencies (< 70 Hz) in the years to come, radiation pressure noise will become the dominant noise source, making high laser power operation a design trade-off. Currently, seismic noise limits low frequency sensitivity, so exploring the technical world of increasing the laser power is a fruitful adventure.

More power introduces a host of radiation pressure and thermally induced side effects that must be addressed for effective interferometer operation. Concerns about the practical difficulties of handling high power effects abounded during Initial LIGO when operating at the design power of 10 W proved more difficult and less straight-forward than expected. To achieve the Advanced LIGO design sensitivity, a whopping 160 W of input power is needed. Without an understanding of the thermal and radiation pressure problems at 10 W, Advanced LIGO becomes all the more daunting of a goal.

The work presented in this dissertation was carried out during Enhanced LIGO to verify and investigate the predicted and unforeseen effects of as much as 25 W of laser power. I present the design and the measurements I made of the performance of two of the interferometer subsystems that are affected by an increase in laser power: the Input Optics and the Angular Sensing and Control. I show that the thermal and radiation pressure effects on these subsystems are well understood and should not pose unsolvable, pick different word problems for Advanced LIGO.

1.1   The Input Optics high power story

The performance of the Initial LIGO Input Optics degraded as the result of absorbing too much heat while the input power ramped up to 7 W. Particular issues that needed to be addressed for any further increase in power included thermal steering of the beam rejected by

the interferometer, a decrease in the optical isolation, and thermal lensing that drove the spatial mode of the beam directed at the interferometer away from optimal. I describe the design of the improved Input Optics which includes less absorptive optical components in order to conquer thermal issues at the source and changes to the design architecture that compensate for any residual effects. I also present the set of measurements I made to characterize their performance with up to 30 W input power. I show that we can expect the Input Optics to perform well for Advanced LIGO.

1.2 The Angular Sensing and Control high power story

Radiation pressure creates torques, a long-known concept, and the optical torque's ability to de-stabilize optical cavities was first recognized in 1991 by Solimeno et al. [1]. However, the theory of radiation pressure's effect on angular mechanical transfer functions was not fully appreciated and published until 2006 by Sidles and Sigg [2]. The concern arised that radiation pressure might be the factor limiting Initial LIGO's ability to increase the input power. Eiichi Hirose showed that the optical torque was present and measurable, but that it was *not* limiting Initial LIGO's power [3].[1] The concern of the optical torque's role in cavity dynamics shifted to Enhanced and Advanced LIGO, which were designed to operate at four times and 20 times the laser power of Initial LIGO, respectively. Lisa Barsotti developed a numerical model of the angular sensing and controls for Enhanced LIGO, specifically including radiation pressure torque. She showed that, in principle, the radiation pressure torque can be controlled without detrimental consequences to the sensitivity of the detector [4]. I implemented Barsotti's theoretical control scheme and measured its performance with up to 20 W of input power, demonstrating a thorough understanding of the principles at work and providing confidence in the ability to control radiation pressure torques in Advanced LIGO. I also improved upon Hirose's

---

[1] In fact, after the Enhanced LIGO laser was installed, and before any changes were made to the ASC, we successfully operated the interferometer with 14 W input power. See Valera Frolov's Nov. 20, 2008 elog.

14

measurement of the optical angular (anti-)spring. And through post-analysis of angular data, I demonstrate the potential of a technique that may be used in Advanced LIGO for reducing the angular control signals.

1.3 Outline of this dissertation

The organization of this dissertation is as follows. Chapter 2 provides the astrophysical motivation...

CHAPTER 2
THE SEARCH FOR GRAVITATIONAL WAVES

The field of ground-based gravitational-wave (GW) physics is rapidly approaching a state with a high likelihood of detecting GWs for the first time. Such a detection will not only validate part of Einstein's general theory of relativity, but initiate an era of astrophysical observation of the universe through GWs. Gravitational waves are dynamic strains in space-time that travel at the speed of light and are generated by non-axisymmetric acceleration of mass. The frequency of the gravitational wave depends on its source. A first detection is expected to witness an event such as a binary black hole/neutron star merger. This chapter provides the theoretical framework of gravitational wave generation and presents various ways to detect GWs, including the current status of an effort to do so. (I conclude with an outline of the content found in the chapters that follow.)

2.1   The theory of gravitational radiation

Gravitational radiation is a perturbation $|h_{\mu\nu}| \ll 1$ to the flat space-time Minkowski metric $\eta_{\mu\nu} = \text{diag}(-1,1,1,1)$. The metric describing space-time in the presence of gravitational radiation is therefore

$$g_{\mu\nu} = \eta_{\mu\nu} + h_{\mu\nu}. \tag{2.1.1}$$

Just as in electrodynamics where one has freedom in choosing the vector potential $\vec{A}$ for calculating the magnetic field $\vec{B} = \vec{\nabla} \times \vec{A}$, one also has freedom in general relativity in choosing the form of $h_{\mu\nu}$ for ease of calculation. A convenient and popular choice is called the transverse-traceless (TT) gauge in which

$$h_{\mu\nu} = \begin{bmatrix} 0 & 0 & 0 & 0 \\ 0 & h_+ & h_\times & 0 \\ 0 & h_\times & -h_+ & 0 \\ 0 & 0 & 0 & 0 \end{bmatrix} \tag{2.1.2}$$

where the $+$ and $\times$ represent two linearly independent polarizations. Without loss of generality, we consider the h_+ polarization in the example that follows.

For a gravitational wave traveling along the z axis, the metric is given by:

$$ds^2 = -c^2 dt^2 + [1 + h_+(t)] dx^2 + [1 - h_+(t)] dy^2. \tag{2.1.3}$$

This says the TT coordinate system is stretched along the x axis and and compressed along the y axis by a factor of

$$\sqrt{1 \pm h_+(t)} \approx 1 \pm \frac{1}{2} h_+(t). \tag{2.1.4}$$

Therefore, the *proper distance* between two free masses located along either the x or the y axes changes by the factor in Eq. 2.1.4; their coordinate separations remain constant. The GW perturbation is a dimensionless strain

$$h = 2 \frac{\Delta L}{L}. \tag{2.1.5}$$

2.2   Sources

Any object with an accelerating mass quadrupole moment generates gravitational waves. The typical strain amplitudes, however, are extremely tiny: a binary system of coalescing $1 M_\odot$ neutron stars in the Virgo Cluster (a distance of 15 Mpc) would produce a maximum GW strain on Earth of only 10^{-21}. Not right–fix this!! The strain is proportional to source mass and velocity, and inversely proportional to distance from the observer:

$$h \approx \frac{GMv^2}{Rc^4} \tag{2.2.1}$$

Consequently, the most promising sources of detectable gravitational waves are nearby, fast-moving, massive astrophysical objects that include

- supernovae
- binary stars (orbiting or coalescing)
- spinning neutron stars
- cosmological/astrophysical background

and can be categorized as producing periodic, burst, or stochastic GWs.

Stably orbiting binary star systems comprised of black holes or neutron stars as well as rapidly spinning non-axisymmetric pulsars are considered periodic sources since they will

17

produce GWs of relatively constant frequency. These reliable sources of GWs require a long integration time to pick out their signal above noise. The Hulse-Taylor binary, for instance, falls into this category. Supernovae are burst sources since the gravitational collapse will produce a short-lived, unmodeled emission of GWs. Binaries in their final tens of milliseconds of inspiral also fall into this category. Finally, the anisotropies in the inflation of the universe together with the hum of all distant astrophysical sources will create a stochastic background of radiation. Coherent cross-correlation between multiple detectors is necessary for measuring the constant amplitude, broad-spectrum GW background.

Directly detecting gravitational radiation from any such source will reveal information that electromagnetic radiation cannot convey. The frequency of the GW tells about the dynamical timescale of the source. Only through GW radiation, for example, can mass and spin properties of a black hole be revealed.

2.3   Methods of detection

- Hulse/Taylor

- Resonant bars

- Pulsar timing

- CMB polarization (B-modes)

- Interferometry

For an approachable overview of the history of the field, including detector design choices and estimated GW strain amplitudes of various sources, refer to Ref. [5].

2.4   State of ground-based interferometry

A network of first generation kilometer-scale laser interferometer gravitational-wave detectors completed its integrated 2-year data collection run in 2007, called S5. The instruments were: the American Laser Interferometer Gravitational-wave Observatories (LIGO)[6], one in Livingston, LA with 4 km long arms and two in Hanford, WA with 4 km and 2 km long arms; the 3 km French-Italian detector VIRGO[7] in Cascina, Italy; and the 600 m German-British detector

GEO[8] in Ruthe, Germany. Multiple separated detectors increase detection confidence through signal coincidence and improve source localization through triangulation.

The first generation of LIGO, known as Initial LIGO, achieved its design goal of sensitivity to GWs in the 40 Hz - 7000 Hz band which included a record strain sensitivity of $2 \times 10^{-23}/\sqrt{\text{Hz}}$ at 155 Hz. However, only the loudest of sources produce enough GW strain to appear in LIGO's band, and no gravitational wave has yet been found in the S5 data. A second generation of LIGO detectors, Advanced LIGO, has been designed to be at least an order of magnitude more sensitive at several hundred Hz and above and include an impressive increase in bandwidth down to 10 Hz, dramatically increasing the chances of detection. The baseline Advanced LIGO design [9] improves upon Initial LIGO by featuring better seismic isolation, the addition of a signal recycling mirror at the output port, homodyne readout, and an increase in laser power from 10 W to 165 W.

To test some of Advanced LIGO's new technologies so unforeseen difficulties could be addressed and so that a more sensitive data taking run could take place, increasing the chances of detection, an incremental upgrade to the interferometers was carried out after S5 [10]. This project, Enhanced LIGO, culminated with the S6 science run from July 2009 to October 2010. An output mode cleaner was designed, built and installed, and DC readout of the GW signal was implemented [11]. An Advanced LIGO active seismic isolation table was also built, installed, and tested [12, Ch. 5]. In addition, the 10 W Initial LIGO laser was replaced with a 35 W laser [13]. Accompanying the increase in laser power, the test mass Thermal Compensation System [14], the Alignment Sensing and Control, and the Input Optics were modified.

As of the writing of this dissertation (September 2011), construction and installation of Advanced LIGO is underway. The vacuum systems are being retro-fitted to accompany the new layout, and at LLO the 165 W laser has been installed. At both sites, the new seismic isolation platforms and multi-level suspension cages are being mass-produced. The By 2012, the first of the suspended mirrors will be installed and testing begun. Simultaneously, VIRGO and GEO
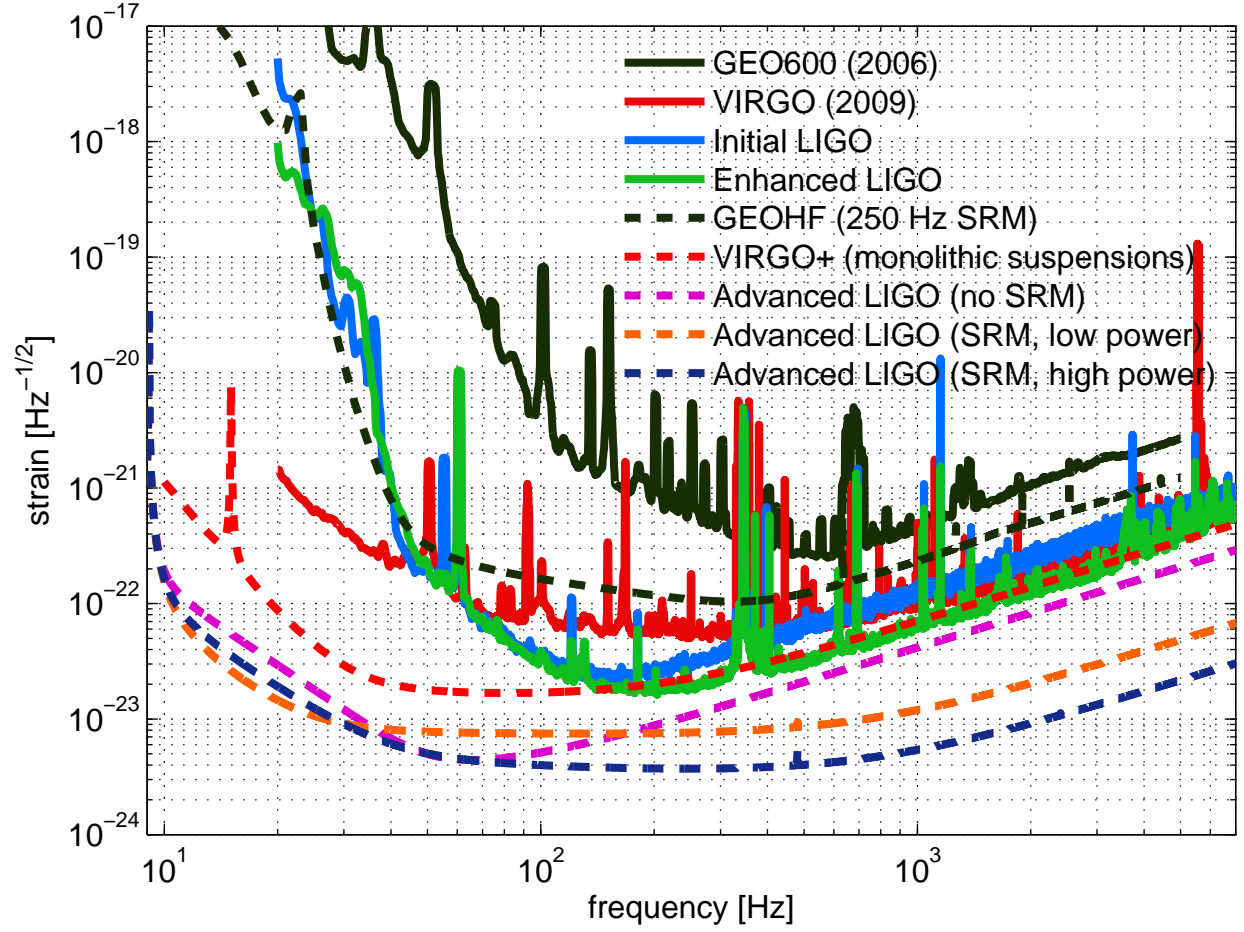
Figure 2-1. Strain sensitivities of LIGO-VIRGO collaboration interferometers.

are both undergoing their own upgrades as well [7] [15]. Figure 2-1 shows the achieved and theoretical future noise curves of this network of ground-based GW detectors.

CHAPTER 3
DESIGN BASICS OF LASER INTERFEROMETERS FOR GRAVITATIONAL-WAVE
DETECTION

I introduce in this chapter some of the basic principles in the design of sensitive intstruments (and the LIGO detectors in particular) to set the stage for delving into the details of the following chapters. I explain why a Fabry-Perot Michelson laser interferometer

3.1   Signal versus noise

The factors that must be considered in the design of any detector can be grouped into two categories: signal and noise. The ability to make a claim of detection is largely dependent on the magnitude of the signal to noise ratio (SNR). An SNR of 8 is desired for detection confidence in LIGO. For laser interferometers, the strength of the GW signal is proportional to the length of the arms and the amount of power in the arms. (See Eq. 8-1.) The change in the distance between the mirrors, ΔL, is bigger for a given strain the longer the arms. And with more circulating power, the greater the amount of power that will show up at the AS port for a given displacement from the dark fringe. Therefore, the two fundamental ways to make a GW produce a bigger signal in an interferometer are: 1) make the arms longer, and 2) increase the circulating power.

No matter how large a signal one might have, it won't be found confidently, or at all, if there is too much noise. The noise itself is best grouped into categories of displacement noise and sensing noise which affect the length of the arms and the measurement of the signal, respectively. Interferometers for GW detection are plagued primarily by displacement noise below 70 Hz and sensing noise above 200 Hz.

In the next sections I will describe briefly the specific types of displacement and sensing noises affecting the sensitivity of laser interferometers. A summary of the noise budget is shown in Fig. 3-1.

3.1.1   Displacement noise

ground motion, thermal noise

Figure 3-1. Noise budget place holder.

seismic noise physically displaces the mirrors, resulting in changes in the length of the arm.

3.1.2 Sensing noise

stray light, shot noise

Shot noise is a quantum mechanical effect of the detection of photons which creates uncertainty in the phase of the light, and therefore the power, at the AS port.

3.2 Measuring GW strain with light

3.2.1 Light as a photon

Consider two wave packets leaving the beam splitter of a Michelson interferometer at the same time, each heading down a different arm. If an appropriately polarized gravitational wave is present, the amount of time the wave packet takes to travel down a stretched arm and back is:

$$t_{rt+} = \frac{2L}{c}\left(1 + \frac{h_+}{2}\right) \tag{3.2.1}$$

Likewise, for a compressed arm the roundtrip travel time is:

$$t_{rt-} = \frac{2L}{c}\left(1 - \frac{h_+}{2}\right) \tag{3.2.2}$$

There is a non-zero $2Lh_+/c$ difference in arrival times at the beam splitter, a quantity one could measure with an accurate stationary clock. This demonstrates intuitively that a laser interferometer can detect gravitational waves.

It should be noted that we had to use the approximation that the gravitational wave wavelength λ_{gw} is much larger than the interferometer arm length L. This means that the temporal variation of $h_+(t)$ is negligible during the time it takes the photon to make its roundtrip. Thus, h_+ is treated as a constant in Eqs. 3.2.1 and 3.2.2.

3.2.2 Light as a wave

The detector at the beam splitter is not a clock, but a photodetector which is sensitive to phase. It would be informative, therefore, to express the difference in arrival times as a difference in phase. To do so, we must move away from the photon model and think about the wave model of light. The light wave's phase is given by $\phi = \omega t$ where t is the proper time. Then, the

difference in phase between the two light beams after each has completed its roundtrip is:

$$\Delta\phi = \phi_{rt+} - \phi_{rt-} = \frac{2L\omega}{c}h_+ \tag{3.2.3}$$

Two time derivatives yields

$$\frac{d^2\Delta\phi}{dt^2} = \frac{2L\omega}{c}\partial_t\partial_t h_+. \tag{3.2.4}$$

It can be shown [16] that the Riemann tensor in the TT gauge is $R_{tkti} = -\frac{1}{2}\partial_t\partial_t h_{ki}$, and gauge invariant. Therefore, our physically measurable quantity can be expressed as being manifestly gauge invariant, proving that a laser interferometer can detect the effect of gravitational waves.

3.3 Power-recycled Fabry-Perot Michelson interferometers

The typical detector configuration is a power-recycled Fabry-Perot Michelson laser interferometer featuring suspended test masses in vacuum as depicted in Figure 3-2. A diode-pumped, power amplified, and intensity and frequency stabilized Nd:YAG laser emits light at 1064 nm. The laser is directed to a Michelson interferometer whose two arm lengths are set to maintain destructive interference of the recombined light at the anti-symmetric (AS) port. An appropriately polarized gravitational wave will differentially change the arm lengths, producing signal at the AS port proportional to the GW strain and the input power. The Fabry-Perot cavities in the Michelson arms and a power recycling mirror (RM) at the symmetric port are two modifications to the Michelson interferometer that increase the laser power in the arms and therefore improve the detector's sensitivity to GWs.

3.4 Controlling the interferometer

The ability of the interferometer to provide a differential arm length signal depends on the many interferometer cavities being locked (define locking!) all at once since it is the light that serves as our probe of arm length. The motion of the mirrors without any control is too large for a locked state to naturally occur. The rms pendular displacement of the mirrors without control is 1 μm, equivalent to a full laser wavelength. The arm length would swing from one free spectral range to the next, never staying put long enough at any particular FSR.
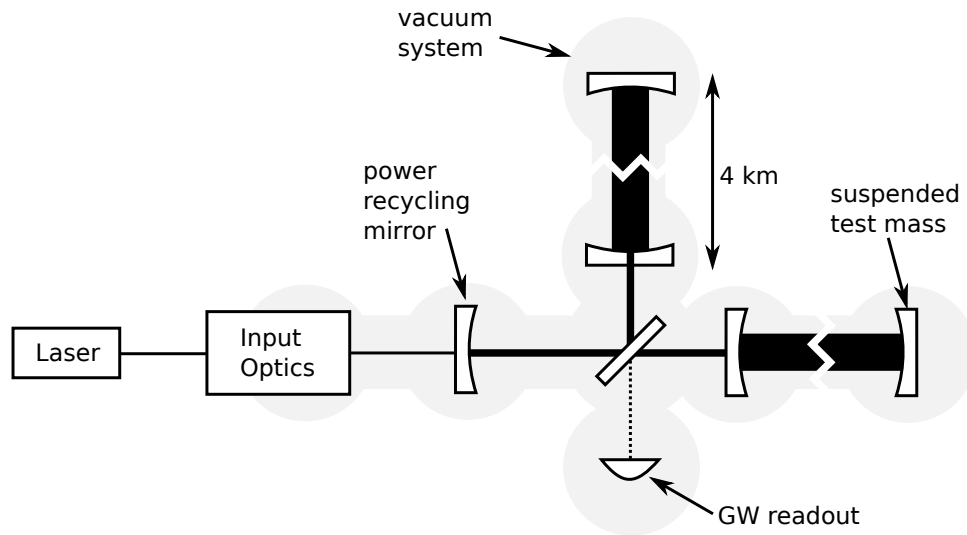
Figure 3-2. Power-recycled Fabry-Perot Michelson laser interferometer.

The motion of the interferometer mirrors must be controlled enough so that resonance is achieved and error signals fall in a linear regime. Since the strain sensitivity is determined by mathematically undoing the (carefully measured) effect of the control system on DARM, control does not directly improve the strain sensitivity. The purpose control serves is to make the strain measurement possible. Control, however, introduces noise so there is a fine balance that must be found between too much and too little control.

Design considerations for the control loops include how much motion at what frequencies can be tolerated, and the signal to noise ratio of the motion sensor.

3.4.1 RF sidebands

3.4.2 Digital Control in LIGO

Although the interferometer is an analog instrument, it is interfaced through a digital control system. The analog sensor signals are sent through an analog-to-digital converter (ADC), digitally filtered, and then sent through a digital-to-analog converter (DAC) before returning to the interferometer's actuators as control signals. The use of a digital control system means complex filters can be more easily implemented than they would with analog electronics, and the potential

There a select few control systems that remain completely analog, like the laser intensity stabilization servo (ISS). When the frequencies of interest extend beyond several tens of thousands of Hz, the use of computers becomes impractical.

3.4.3 Mirror suspension and actuation

The primary interferometer optics are suspended in vacuum so that they act like free masses at the frequencies in the GW detection band. Each mirror is hung from a single xx m diameter wire that loops around the bottom of the barrel of the mirror as shown in Fig. 6-1. Stand-offs glued just above the mirror's center of mass on both sides of the barrel mark the final point of contact of the wire with the mirror, and both ends of the wire are clamped to the top of a suspension cage.

Minimal contact with the mirrors is necessary to avoid thermal noise. Therefore, the suspensions provide minimal damping to the mirrors. Damping for the large optics is instead achieved electronically through the use of optical levers. Figure 3-3 shows the open loop gain of the optical lever servo, demonstrating that it provides velocity damping only (no DC control) between 0.2 Hz and 2 Hz.

Each mirror is equipped with four optical sensor and electro-magnetic (OSEM) actuators for providing control to the mirror. Magnets arranged to form the four corners of a square are glued on the mirror's back surface, and the OSEM units envelop them. Length control of the cavities, for instance, sends current of the same magnitude through each coil on a given mirror to provide a piston force for changing the mirror's position.

The OSEMs provide local damping when the interferometer is not locked.

3.5   More Laser Power

Shot noise results from an uncertainty in the arrival time of photons on a detector:

$$P_{shot} = \sqrt{2h_p\nu P_{DC}} \ \text{W}/\sqrt{\text{Hz}} \tag{3.5.1}$$

where P_{DC} is the DC power on the wavefront sensor, h_p is Planck's constant and ν is the frequency of the laser light.
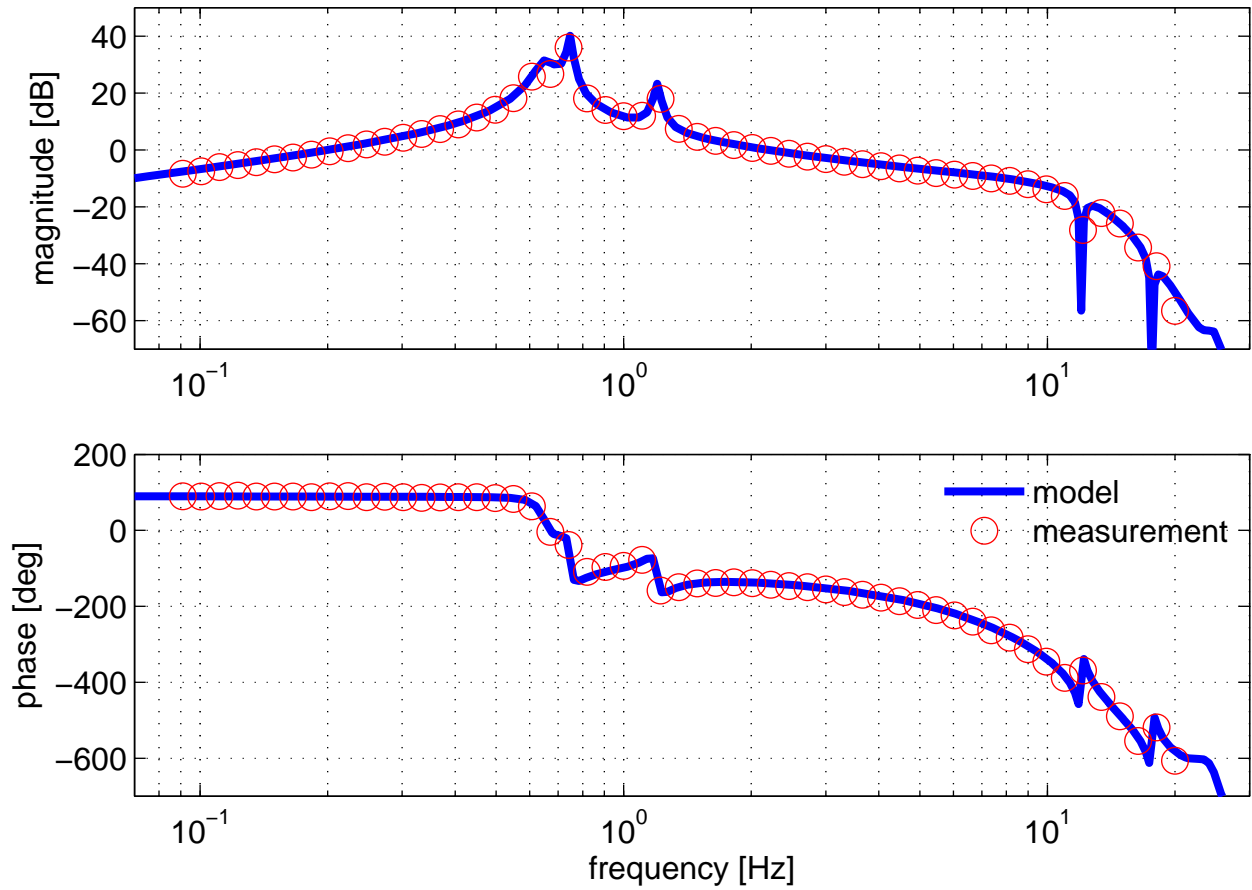
Figure 3-3. ETMX pitch optical lever open loop transfer function. Uses the filters in the oplev servo filter bank, only (no coil output filters). The model of the plant is tuned to match the data, resulting in a pitch resonance of 0.65 Hz and a damping factor of $\gamma = 0.02$. The UGF is at 2.2 Hz and the phase margin is $38°$.

CHAPTER 4
INPUT OPTICS

Insert IO paper here.

CHAPTER 5
THE ANGULAR MOTION OF THE INTERFEROMETER

For light to resonate in the interferometer, the mirrors need to point at one another and remain stationary with respect to this pointing. In practice, however, the mirrors are subject to external disturbances. Each torque produces an angular displacement of the mirror as governed by the mirror's torque to angle transfer function and results in either a static or dynamic misalignment.

The dynamic misalignments arise from torque introduced through the suspension from ground motion and through the actuators from an unbalanced piston force. Both of these torques create an angular motion independent of the state of the mirror's pointing. Radiation pressure torque, however, stands apart; its effect depends on the pointing of the mirror. A consequence is that even when all of the mirrors are perfectly aligned at all frequencies, the simple existence of light in the interferometer makes the arm cavities statically unstable when high enough laser powers are used.

This chapter discusses the causes of mirror angular displacement and the effects of residual mirror motion on the interferometer. Background material is provided as necessary, such as the dynamics of torsion pendula, and the geometric eigenfunctions of linear cavities. The need for an Angular Sensing and Control subsystem will be apparent.

5.1   Overview of interferometer alignment

There are 8 mirrors whose pitch and yaw angles must be sensed and controlled. The sensing is accomplished by 8 sensors, which fall into three groups:

- camera image (BS)
- quadrant photodiodes (QPDX, QPDY)
- wavefront sensors (WFS1, WFS2, WFS3, WFS4)

The alignment of these mirrors using these sensors can be simplified by considering the interferometer alignment as happening in two basic units: the input beam and the power recycled Fabry-Perot Michelson. The alignment of the latter is nearly self-contained and can in fact be

28

compacted down to a representative single mirror. The remaining jobs are to align the input beam and this "single mirror" to one another and to keep the y-arm perpendicular to the x-arm.

The self-contained alignment of the power recycled Fabry-Perot Michelson is realized through the set of wavefront sensors (WFS), whose principle of operation is described in Section 5.5. The pitch and yaw motions of the five mirrors in this unit, ETMX, ETMY, ITMX, ITMY, and the PRM, are sensed by the pitch and yaw of five WFS signals, WFS1Q, WFS2I, WFS2Q, WFS3I, and WFS4I, where I and Q denote in-phase and quadrature demodulation, respectively. These WFS look at light at the AS port, at the reflected port, and in the power recycling cavity. They control the relative motions of these five mirrors up to a couple Hz.

The MMT-directed input beam and the interferometer "mirror" need to be aligned so that the input beam is perfectly reflected upon itself. The input beam follows the interferometer on about minute time scales, and at higher frequencies the interferometer follows the input beam. The low frequency matching of the input beam pointing to the interferometer "mirror" is realized through the pitch and yaw signals of QPDX, a QPD which monitors the position of the light transmitted through the x-arm, and the pitch and yaw signals of a camera that monitors the beam location on the beam splitter. These two alignment sensors adjust the pointing of MMT1 and MMT3 on about minute time scales. An example of the BS camera image is shown in Fig. 5-1. The higher frequency matching of the input beam pointing to the interferometer is achieved by the reflected port Fabry-Perot Michelson wavefront sensors, up to a couple Hz.

The one additional step needed for full interferometer alignment is to maintain the orthogonality of the y-arm to the x-arm as the x-arm and input beam together move around. This is accomplished through the pitch and yaw signals of QPDY, the QPD that monitors the light transmitted through the y-arm, which sense how the beam splitter should be pointed. [1]

All mirror angles are of course interdependent and they must track each other. However, a rough hierarchy of who follows who can be established since ultimately the interferometer is

---

[1] QPDX also sends a signal to the BS to compensate for whatever it has MMT3 do.
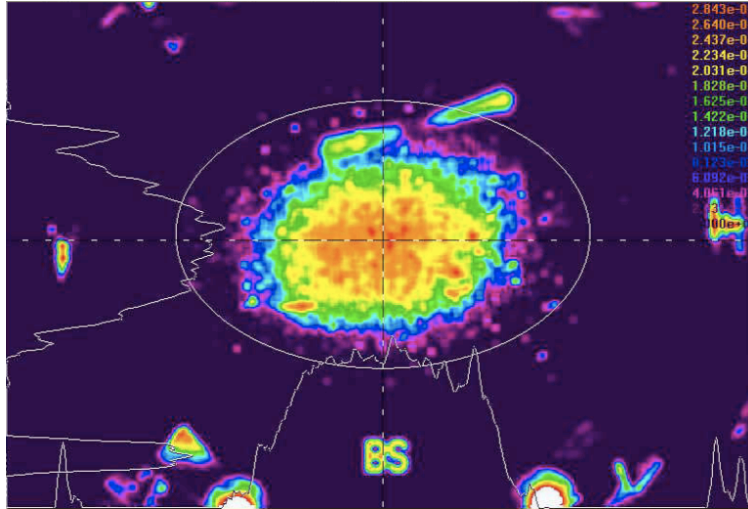
Figure 5-1. Image of beam on beam splitter as used in the beam centering servo. The beam appears stretched because the camera's viewing angle is at 45° with respect to the mirror surface. The color scale is arbitrary.

bolted to the ground and necessarily maintains some DC orientation. This orientation comes from QPDX and QPDY, which are physically attached to piers standing on the ground and force the beams transmitted through the ETMs to stay put at a certain location on their sensors. In all, the input beam must make it to those two exact places and the other mirrors are left to line themselves up accordingly. A diagram of this alignment scheme is in Fig. 5-2.

This alignment process involving the WFS, QPDs, and BS camera relies on the entire interferometer already being locked. It manages the continuous fine-tuning of mirror angles so that maximal power buildup in the interferometer is maintained, and so that the interferometer does not wander from its linear operating point. How to achieve the initial alignment of all of the mirrors is an interesting process in itself and is documented in Appendix 10.3.

5.2   Sources of mirror motion

If the interferometer can be aligned well enough by hand for the initial lock to be achieved, one might wonder why the need for continuous tweaking thereafter. The answer is that there is a continuous stream of changing torque inputs to the mirrors that cause them to twist and turn in pitch and in yaw. Some torque inputs exist regardless of the state of the interferometer, while
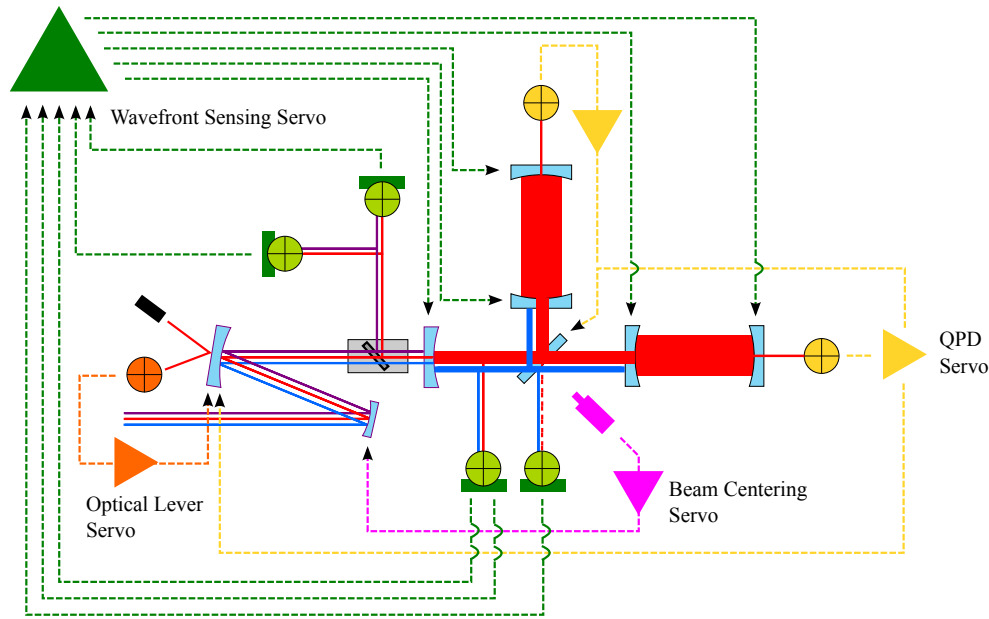
Figure 5-2. Schematic of the alignment sensing and control system, showing the placement of sensors and which mirrors they control. The QPD servo and Beam Centering Servo (BCS) together direct the input beam to follow the FPM unit on minute time scales. The QPD servo additionally keeps the BS properly directing light into the y-arm. The wavefront sensing servo maintains the alignment of the FPM mirrors with respect to each other up to several Hz. Each of the seven large optics has its own velocity damping optical lever servo.

others are a direct consequence of the control systems. The primary torque inputs are introduced here, and further discussion of some of them is found later in the chapter. The list includes:

- ground motion
- coil actuators (length to angle)
- radiation pressure
- noise impression from the angular control system

5.2.1 Ground motion

The most egregious of these torque inputs is ground motion that makes its way through the multiple stages of seismic isolation to the mirror suspensions. This is the only source of angular motion that is present regardless of the state of interferometer operation, and it is also AC damped at all times for each of the large optics through optical lever witnesses. Keeping the mirrors quiet enough with respect to their local ground is necessary to allow for the initial
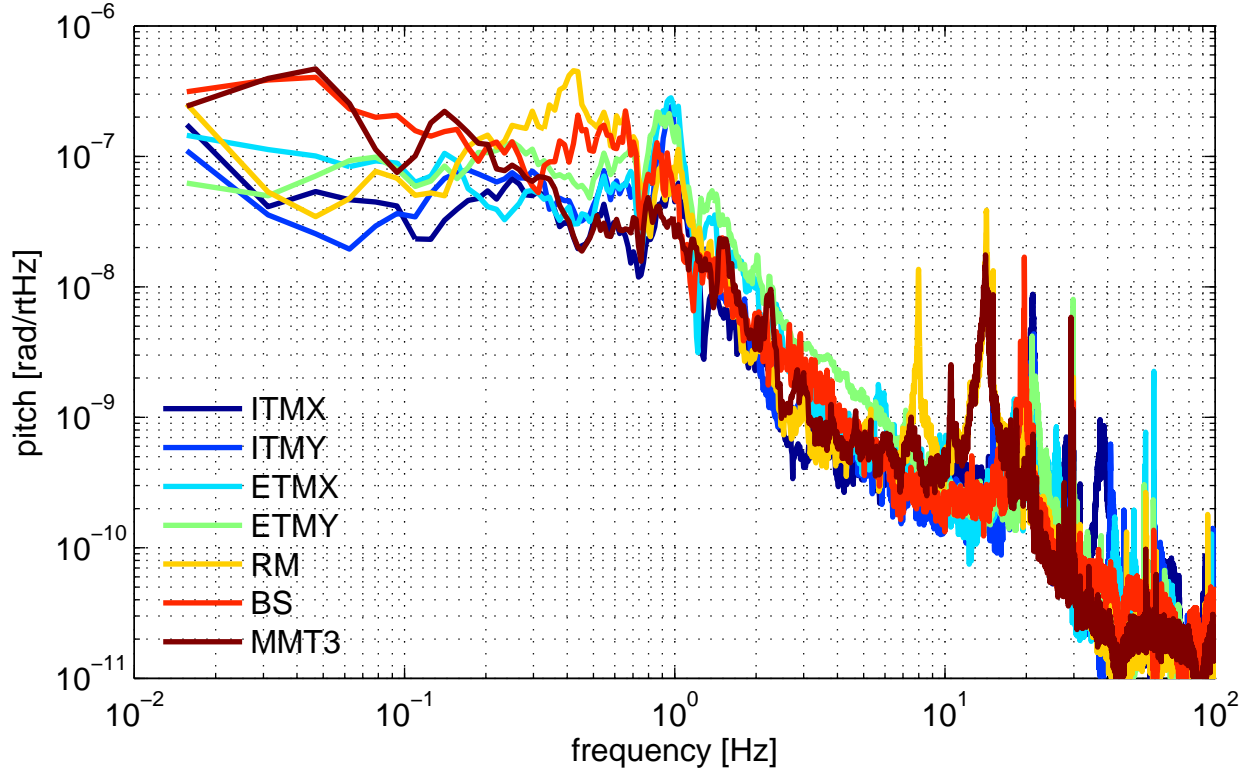
Figure 5-3. Typical angular motion of the core suspended mirrors in the absence of interferometric control. Velocity damping provided by the OSEMs and the optical levers is present. Once the interferometer is locked, the OSEM damping is ramped off.

locking of the interferometer, so each suspended optic, small and large, is quieted by its OSEM signals during the initial locking stages. An example of the shape and amount of velocity-damped angular motion experienced by the core optics due to seismic noise during a relatively quiet seismic time is shown in Fig. 5-3. The rms mirror motion is of the order 10^{-7} rad. This is the motion that needs to be controlled interferometrically.

5.2.2   Coil actuators

The imperfect piston drive of the actuators on the rear of the test masses due to length control is another torque input, albeit inconsequential. The length of the cavities is carefully controlled (that's what we strive to be most sensitive to!) and any imbalances between the four electromagnets on a single mirror will create a coupling from length drive to angle (L2A). This effect is measurable, but is carefully tuned out through selecting appropriate digital gains for each

of the coils. Typically, the gain variation from unity is up to 10%. The residual is about 1%. For the typical rms length drive of 1 μmon a core optic and osems separated by a distance of $\sqrt{2}R$ where R is the radius of the optic, the 1% L2A coupling results in a 10^{-8} radian displacement:

$$\theta = \frac{0.01 * 10^{-6} \text{ m}}{\sqrt{2} * 0.125 \text{ m}} \approx 10^{-8} \text{ rad.} \tag{5.2.1}$$

5.2.3 Radiation pressure

Radiation pressure creates a torque when the beam impinges the mirror off-center. The force on the mirror due to radiation pressure is derived from the change in momentum of a photon upon reflection off the mirror and results in:

$$F_{rp} = \frac{2P}{c} \tag{5.2.2}$$

where P is the power of the light reflected by the mirror and c is the speed of light. Assuming the beam of photons strikes the mirror perpendicular to its surface, the torque exerted on a mirror due to radiation pressure is

$$\tau_{rp} = \frac{2Px}{c} \tag{5.2.3}$$

where x is the distance of the beam from the mirror's center of mass. For a 40 kW beam 1 mm off-center, the torque is on the order of 10^{-7} Nm, corresponding to an angular displacement of the order 10^{-7} rad as determined by the pendulum torque to angle transfer function (see 6.1).

Amongst the various torque inputs, radiation pressure plays a unique role in mirror motion because the torque it exerts depends on the angles of the mirrors. This is a result of the geometric coupling between beam displacements and mirror angles as will be shown in the next chapter. Radiation pressure therefore acts as an angular spring. It is best treated not as an external torque, but as a modification to the pendulum torque to angle transfer function. Part of the next chapter dedicates a discussion to this matter. In all, radiation pressure shapes the angular dynamics of the mirrors in LIGO and plays an important role in the design of an angular control system.

5.2.4   Noise from angular control

The angular control system, which strives to counteract the above torque inputs to reduce angular motion, introduces angular mirror motion itself. The primary way it contributes noise is through imperfect sensing of the angular displacements. The control system also impresses input beam motion on the mirrors. These issues and others are explained in more detail in 5.4.

5.3   Tolerance for angular motion

The requirements for how much motion is tolerable stem from two effects of misalignment that directly couple to strain sensitivity: power build-up degradation, and angle to length coupling. The misalignment tolerances are dictated by what is necessary to prevent the strain sensitivity of the perfectly aligned interferometer from degrading by more than 0.5% in the detection band of 40-7000 Hz [17].

Since the strain sensitivity is proportional to the power buildup (see Eq. 8-1), a decrease in circulating power directly results in a decrease of shot-noise-limited DARM. Differing power fluctuations in the two arm cavities results in a changing contrast defect, a difference in the amount of light returning from one arm compared to the other, which increases the shot noise at the AS port. Too large of power fluctuations in the power recycling cavity makes for inconsistent signal to noise ratios for the signals that depend on sideband power. To maintain a power buildup within 1% of maximum, the core optics must have an angular displacement of less than 10^{-8} rad rms with respect to the cavity axis [18]. The derivation of power buildup as a function of mirror angle displacement is found in Appendix 10.2.

work this paragraph in somewhere The idea is that when the axis of rotation of a mirror coincides with the center of the beam, any tilt of the mirror about this axis does not affect the path length of the reflected beam. However, if there is a mismatch between rotation axis and beam location, then the light will pick up a longitudinal phase shift when the mirror is tilted. During a full interferometer lock, this is recorded by DARM.

When the beam is located a distance x away from the center of the mirror, an angular displacement of the mirror θ about its center results in a path length change of the beam

$$\Delta L = x * \theta \qquad (5.3.1)$$

which has a direct impact on DARM. Therefore, the alignment specifications must include not only tolerable levels of angular motion, but requirements for the physical centering of the beam spots on the mirrors. As detailed in Ref. [18], the beams must be centered on the core optics within 1 mm. At DC, for x = 1 mm and $\theta = 10^{-7}$ rad, $\Delta L = 10^{-10}$ m which is four orders of magnitude below the DARM rms of 10^{-6} m. Convolve my bsm spectra and residual mirror motion spectra to show example.

5.4   Angular control limitations

The limits for how good we can do in controlling the angular motion of the interferometer are governed by how well we are able to sense the angular motion. Several of the wavefront sensors' signals are dark-noise-limited above 20-25 Hz, as seen in Fig. 5-4. And depending on the power level, WFS1Q may instead be limited by shot noise (see Eq. 3.5.1). Any control signal derived from frequencies in the sensing noise limited regime will impress the sensor noise on the mirrors. This cannot be avoided entirely in the presence of feedback, but can be mitigated by including amongst the control filters a steep cut-off beginning at the sensor noise frequencies.

Besides the sensing noise, there is also sometimes real signal that results in more harm than good when used as feedback. The HAM seismic isolation tables used by the Input Optics (the core optics are suspended from BSC tables) have stack modes of xx Hz that ring up the MMTs. At low frequencies, around 1 Hz, some of the WFS signals are dominated by these angular fluctuations of the input beam. The resulting attempt of the mirrors to follow the input beam jitter leads to a magnification of the motion because of the drastically different length scales. Large power fluctuations in both arms and the power recycling cavity ensue, leading to departure from the linear error signal regime and often lock loss.
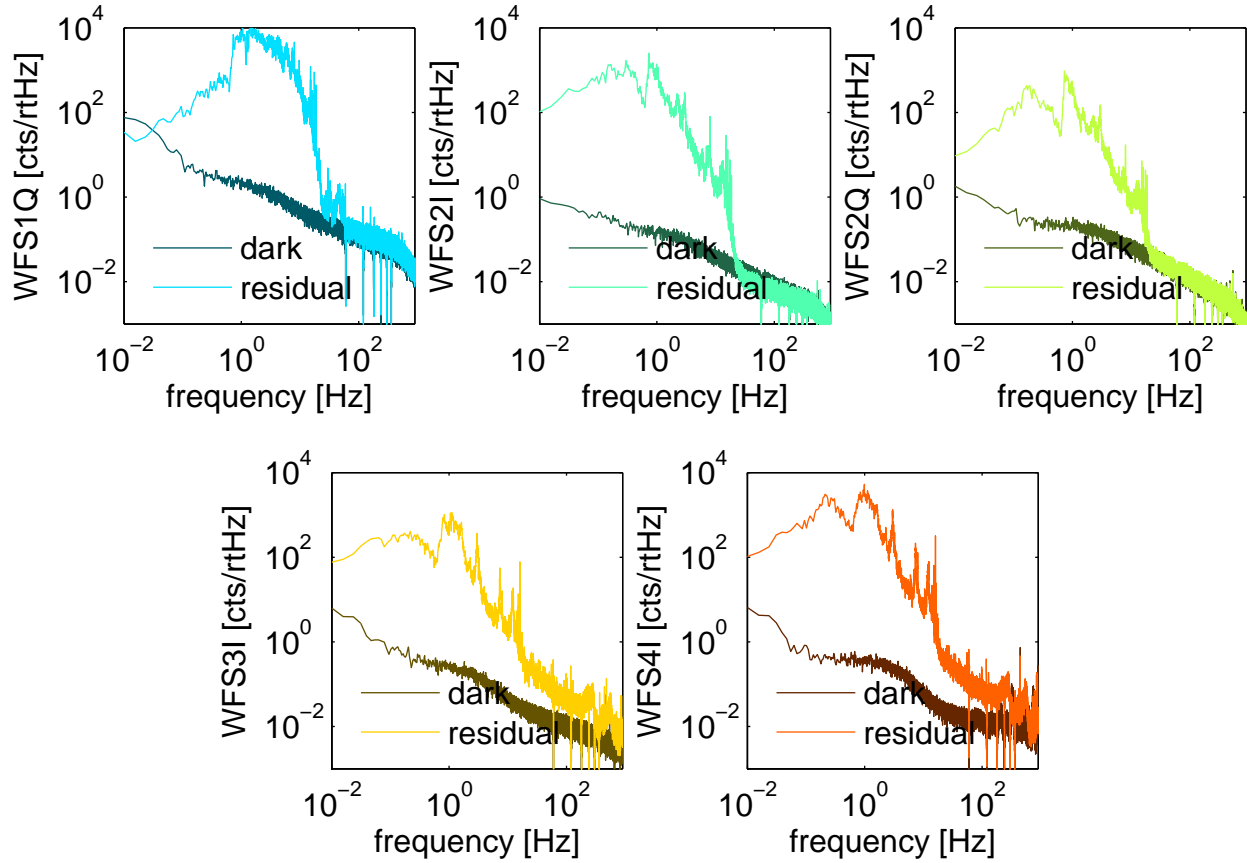
Figure 5-4. WFS dark noise compared to typical error signal. Include shot noise, too, especially for WFS1. The excess signal above the dark noise in WFS3I and WFS4I from 20 Hz on is likely acoustic noise, although this has not been verified. WFS1 and WFS2 are on a floating table in a sound proof chamber, while WFS3 and WFS4 are on a non-seismically isolated table without a sound proof enclosure.

Other limitations to the reduction of mirror motion result from the nature of control loops. The cut-off filter, for example, reduces the phase margin of the open loop gain, necessarily pushing down the unity gain frequency (UGF) and therefore the magnitude of suppression at all frequencies below the UGF. A less aggressive cut-off filter, while improving the servo's stability and allowing for higher overall gains, leads to more impression of sensing noise on the optics. Also, when the phase margin of the loop is low, some mirror motion is amplified through gain peaking.

5.5   Wavefront sensing

Describe modes, reference sidebands, Gouy phases; give FP cavity example.

CHAPTER 6
DYNAMIC RESPONSE OF COUPLED PENDULA

In order to design a control system that reduces the angular motion of the interferometer mirrors to the levels necessary for stable interferometer operation and minimal impact on strain sensitivity, the angular response of the mirrors to external torque must be fully understood. The suspended mirrors themselves are nothing more than torsion pendula. However, the torque induced by radiation pressure couples the angular motion of the mirrors in a power dependent way, complicating the plant for which controls must be designed. Namely, radiation pressure torque has the effect of breaking the symmetry of the equations of motion of each of the mirrors. Since Enhanced LIGO embarks on the path of increasing the laser power, examining the effect of radiation pressure torque in detail is warranted. Here, we review the dynamics of a torsion pendulum and the geometry of a linear cavity, and conclude with the derivation and implications of a set of eigenfunctions that diagonalize the linear cavity's response to radiation pressure. The torque to angle transfer functions of the new eigenmodes are modified such that one mode is statically unstable at Enhanced LIGO powers.

6.1   The mirror as a torsion pendulum

The mirrors in LIGO may be regarded as torsion pendula. Each mirror is suspended from a single xx m diameter wire that loops around the bottom of the barrel of the mirror as shown in Fig. 6-1. Stand-offs glued just above the mirror's center of mass on both sides of the barrel mark the final point of contact of the wire with the mirror, and both ends of the wire are clamped to the top of a suspension cage. The mirror is free to twist an angle θ about a horizontal axis passing through its center of mass to create motion in *pitch* and about a vertical axis passing through its center of mass to create a motion in *yaw*.

The angular equation of motion of the mirror is governed by the sum of all torques on the mirror. First, let's consider the most simplistic scenario where there is only a pendulum restoring torque $\tau_p = -\kappa_p \theta$, where κ_p is the pendulum's torsional constant. The equation of motion is

$$I\ddot{\theta} + \kappa_p \theta = 0, \tag{6.1.1}$$
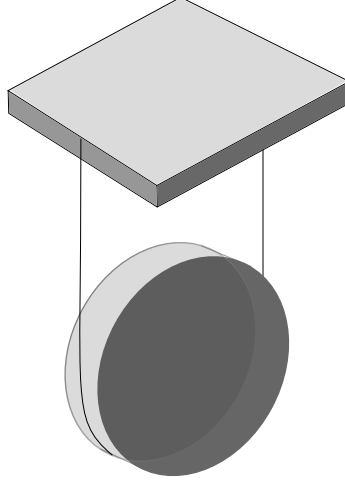
Figure 6-1. Cartoon of a LIGO suspension. Improve this.

which has a solution of $\theta(t) = \sin(\omega_0 t)$, where $\omega_0 = \sqrt{\kappa_p/I}$ is the resonant angular frequency and I is the mirror's moment of inertia. The pendulum torsional constant serves to make the mirror oscillate indefinitely about its equilibrium position upon the slightest of displacements.

6.1.1 Torque to angle transfer function of a pendulum

We are particularly interested in the pendulum's response to an external torque, such as seismic noise. In order to calculate the torque to angle transfer function, we must include an external torque term, τ_{ext}, in the equation of motion:

$$I\ddot{\theta} + \gamma\dot{\theta} + \kappa_p\theta = \tau_{ext}. \tag{6.1.2}$$

Here, we have also introduced a velocity damping term, γ, to best model reality. Taking the Laplace transform to convert from the time domain to the frequency domain, we have:

$$Is^2\Theta + \gamma s\Theta + \kappa_p\Theta = \tau_{ext} \tag{6.1.3}$$

where s is a complex parameter. The transfer function is then defined as

$$H(s) := \frac{\Theta(s)}{\tau_{ext}(s)} = \frac{1}{Is^2 + \gamma s + \kappa_p}. \tag{6.1.4}$$

We are only interested in examining the transfer function for a pure sine wave excitation, $e^{i\omega t}$, so we substitute $s = i\omega$ to get

$$H(\omega) = \frac{1/I}{\omega_0^2 - \omega^2 + i\gamma\omega/I}. \tag{6.1.5}$$

The resonant frequency of this damped system can be computed by finding the ω at which the amplitude of the transfer function, $[I^2[\omega^2 - \omega_0^2]^2 + \gamma^2\omega^2]^{-1/2}$, is maximized:

$$\omega_{res} = \sqrt{\omega_0^2 - \frac{\gamma^2}{2I^2}}. \tag{6.1.6}$$

We note that damping serves to reduce the resonant frequency.

A quantity that is more familiar than γ for describing the losses of a system with a real resonance is the quality factor, $Q := \omega_{res}/\text{FWHM}$, where FWHM is that computed for the amplitude squared of the transfer function. When the losses are small, $\omega_{res} \approx \omega_0$ and FWHM $\approx \gamma/I$ (see Feynman 23-4). The quality factor is then well approximated by $Q = \sqrt{\kappa_p I}/\gamma$. The transfer function written in terms of Q is

$$H(\omega) = \frac{1/I}{\omega_0^2 - \omega^2 + i\omega\omega_0/Q}. \tag{6.1.7}$$

Figure 6-2 shows the pendulum torque to angle transfer function (for pitch) using the parameters of a LIGO core optic. For external torques applied to the mirror above its resonant frequency, the mirror acts like a free mass, one that is not held in place by suspension wires nor subject to damping. For torques applied to the mirror below its resonant frequency, the mirror's angle is determined by the inverse of the torsional constant.

6.2 The radiation pressure angular spring

The geometric axis of a cavity formed by two spherical mirrors is dictated by the line joining the centers of the "spheres" created by the two mirrors. Only if the mirrors are pointed directly at one another will the cavity axis pass through the centers of the mirrors. Should a laser beam resonate in the cavity, it will do so along this geometric axis. Thus, if the mirrors are tilted away from one another, the beam spot on each mirror will not be centered. The relationship between the positions of the beams on the mirrors relative to center, x_i, and the angles of the mirrors, θ_i, is
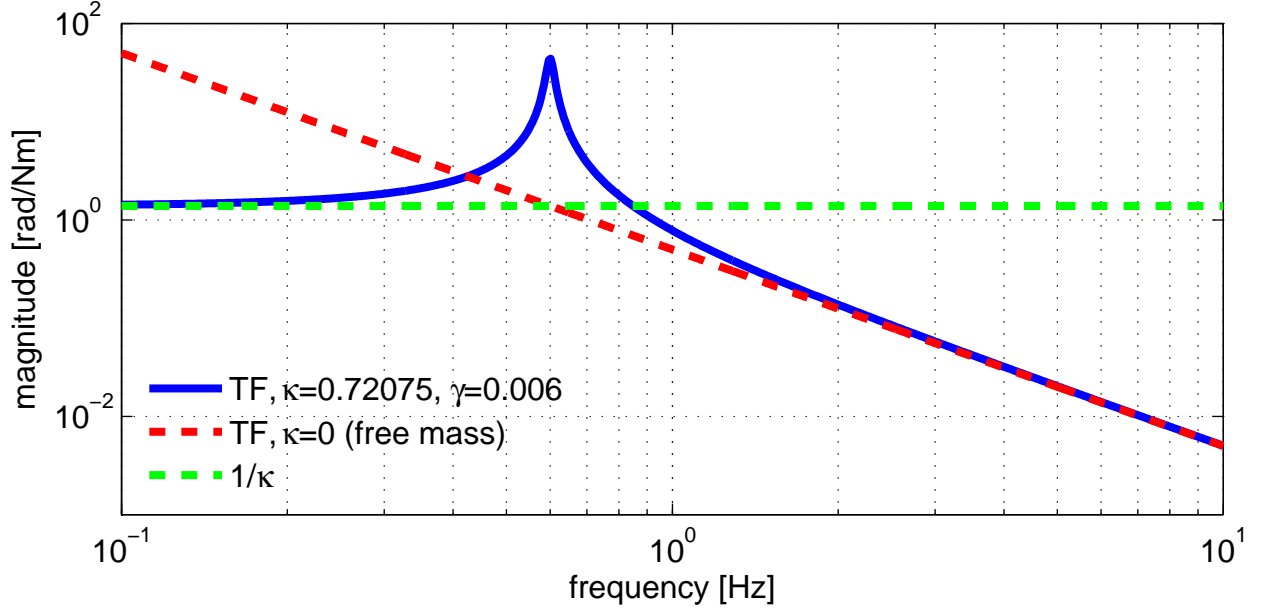
Figure 6-2. Torque to pitch transfer function of a LIGO core optic (blue). The optic acts like a free mass at high frequencies (red) and the DC magnitude of the transfer function is determined by the inverse torsional constant (green). A damping constant $\gamma = 0.006$ ($Q = 32$) was selected for pictorial representation only. The resonant frequency of LIGO core optics in yaw is 0.5 Hz.

given by:

$$\begin{bmatrix} x_1 \\ x_2 \end{bmatrix} = \frac{L}{1 - g_1 g_2} \begin{bmatrix} g_2 & 1 \\ 1 & g_1 \end{bmatrix} \begin{bmatrix} \theta_1 \\ \theta_2 \end{bmatrix}. \tag{6.2.1}$$

The g-factor is defined as $g_i = 1 - R_i/L$ where R_i is the radius of curvature of each of the mirrors, respectively, and L is the length of the cavity.

We saw in the previous chapter that the radiation pressure torque on a mirror depends on the position of the beam on the mirror, $\tau_{rp} = 2Px/c$ (Eq. 5.2.3). Based on Eq. 6.2.1 the radiation pressure torque on a mirror that is part of a Fabry-Pérot cavity is therefore dependent on the angle of both the mirror of interest and the second mirror forming the cavity:

$$\begin{bmatrix} \tau_{rp,1} \\ \tau_{rp,2} \end{bmatrix} = \frac{2PL}{c(1 - g_1 g_2)} \begin{bmatrix} g_2 & 1 \\ 1 & g_1 \end{bmatrix} \begin{bmatrix} \theta_1 \\ \theta_2 \end{bmatrix}. \tag{6.2.2}$$

This is more succinctly expressed as

$$\vec{\tau}_{rp} = -\mathbf{K_{rp}}\vec{\theta}, \tag{6.2.3}$$

where $\mathbf{K_{rp}}$ is the *torsional stiffness matrix*. Equation 6.2.3 is the expression that describes the radiation pressure angular spring.

6.2.1 Diagonalizing the modified equations of motion

The radiation pressure spring modifies the pendulum angular equation of motion and therefore the torque to angle transfer function through the addition of an angle-dependent torque term. Re-writing Eq. 6.1.2 in matrix form and with the radiation pressure spring term, the two equations that describe the motion of two mirrors forming a Fabry-Pérot cavity is:

$$\mathbf{I}\ddot{\vec{\theta}} + \gamma\dot{\vec{\theta}} + \kappa_\mathbf{p}\vec{\theta} - \frac{2PL}{c(1 - g_1 g_2)} \begin{bmatrix} g_2 & 1 \\ 1 & g_1 \end{bmatrix} \vec{\theta} = \vec{\tau}_{ext}. \tag{6.2.4}$$

$\mathbf{I}$, γ, and κ_p are 2×2 diagonal matrices and $\vec{\theta}$ and $\vec{\tau}_{ext}$ are 2×1 vectors as in the previous section. Due to the non-diagonal matrix in Eq. 6.2.4, the motions of each of the mirrors forming the cavity are tied to one another. The natural way to work with such a system is to rotate the coupled equations into a new basis. The resulting de-coupled equations of motion will described specific combinations of mirror tilts instead of individual mirrors. Vectors in the rotated basis are written with primes.

In order to decouple the two equations of Eq. 6.2.4, we need to diagonalize $\mathbf{K_{rp}}$. The subscripts a and b are used to denote the elements of the diagonalized basis, to contrast the 1 and 2 which denote the mirror basis. Ignoring the constants of matrix $\mathbf{K_{rp}}$, its eigenvalues are

$$\lambda_a = \frac{g_1 + g_2 + \sqrt{(g_1 - g_2)^2 + 4}}{2} \tag{6.2.5}$$

$$\lambda_b = \frac{g_1 + g_2 - \sqrt{(g_1 - g_2)^2 + 4}}{2} \tag{6.2.6}$$

41

and its eigenvectors are

$$\vec{v}_a = \begin{bmatrix} 1 \\ \frac{g_1 - g_2 + \sqrt{(g_1 - g_2)^2 + 4}}{2} \end{bmatrix} \qquad (6.2.7)$$

$$\vec{v}_b = \begin{bmatrix} \frac{-g_1 + g_2 - \sqrt{(g_1 - g_2)^2 + 4}}{2} \\ 1 \end{bmatrix}. \qquad (6.2.8)$$

Therefore, the matrix

$$\mathbf{S} = \begin{bmatrix} \vec{v}_a & \vec{v}_b \end{bmatrix} = \begin{bmatrix} 1 & \frac{-g_1 + g_2 - \sqrt{(g_1 - g_2)^2 + 4}}{2} \\ \frac{g_1 - g_2 + \sqrt{(g_1 - g_2)^2 + 4}}{2} & 1 \end{bmatrix} \qquad (6.2.9)$$

diagonalizes $\mathbf{K_{rp}}$ such that

$$\mathbf{S}^{-1}\mathbf{K_{rp}}\mathbf{S} = \mathbf{D} = \begin{bmatrix} \lambda_a & 0 \\ 0 & \lambda_b \end{bmatrix} = \begin{bmatrix} \frac{g_1 + g_2 + \sqrt{(g_1 - g_2)^2 + 4}}{2} & 0 \\ 0 & \frac{g_1 + g_2 - \sqrt{(g_1 - g_2)^2 + 4}}{2} \end{bmatrix}. \qquad (6.2.10)$$

The matrix of eigenvectors, $\mathbf{S}$, is the basis transformation matrix. It serves to define the torque and angle vectors in the new basis. For example,

$$\vec{\theta}' = \begin{bmatrix} \theta_a \\ \theta_b \end{bmatrix} = \mathbf{S}^{-1} \begin{bmatrix} \theta_1 \\ \theta_2 \end{bmatrix} = \mathbf{S}^{-1}\vec{\theta}. \qquad (6.2.11)$$

Rearranging Eq. 6.2.10 to the form $\mathbf{K_{rp}} = \mathbf{SDS}^{-1}$ and substituting it into Eq. 6.2.4, we have:

$$\mathbf{I}\ddot{\vec{\theta}} + \gamma\dot{\vec{\theta}} + \kappa_{\mathbf{p}}\vec{\theta} - \frac{2PL}{c(1 - g_1 g_2)}\mathbf{SDS}^{-1}\vec{\theta} = \vec{\tau}_{ext} \qquad (6.2.12)$$

Multiplying on the left by $\mathbf{S}$, taking advantage of the diagonal $\mathbf{I}$, γ, and κ_p matrices, and using $\mathbf{S}$ to change the basis of each of the vectors, the de-coupled equations of motion are:

$$\mathbf{I}\ddot{\vec{\theta}}' + \gamma\dot{\vec{\theta}}' + \kappa_{\mathbf{p}}\vec{\theta}' - \frac{2PL}{c(1 - g_1 g_2)} \begin{bmatrix} \lambda_a & 0 \\ 0 & \lambda_b \end{bmatrix} \vec{\theta}' = \vec{\tau}'_{ext}. \qquad (6.2.13)$$

42

Table 6-1. Geometric parameters of the LIGO arm cavity eigenmodes. x_i are the beam locations on the mirrors relative to center, a is the cavity axis displacement at the waist, and α is the cavity axis angle with respect to a line joining the centers of the mirrors. Differences between LLO and LHO arise from the mirrors at each site having different radii of curvature. Quantities are expressed as a function of the amount of tilt in a particular mode.

cavity parameter	unit	LLO $\vec{v}_a$ mode	LLO $\vec{v}_b$ mode	LHO $\vec{v}_a$ mode	LHO $\vec{v}_b$ mode
$|x_1|$	mm/urad	9.88	2.44	8.20	2.51
$|x_2|$	mm/urad	10.84	2.22	9.35	2.20
$|a|$	mm/urad	10.17	1.01	8.48	1.34
$|\alpha|$	urad/urad	0.24	1.17	0.29	1.18

The radiation pressure spring constant, κ_{rp}, is

$$\kappa_{rp} = -\frac{2PL}{c(1 - g_1 g_2)}\lambda \tag{6.2.14}$$

where $\lambda = \lambda_a$ or λ_b, depending on the mode in question.

The angular motion of the Fabry-Pérot cavity is no longer described on an individual mirror basis. Due to radiation pressure, the cavity is treated as a unit and the two orthogonal modes of angular motion are combinations of the two mirrors' angles. The eigenvectors $\vec{v}_a$ and $\vec{v}_b$ describe these two sets of orthogonal mirror tilts, and the eigenvalues λ_a and λ_b (along with their common constants) quantify the magnitude of the radiation pressure torsional spring constant for each of the modes. While the equations of motion had been identical for each of the individual mirrors, the decoupled equations in the presence of radiation pressure breaks that symmetry.

Table 6-1 outlines the characteristics of these two eigenmodes for the specific geometry of the LIGO arm cavities. The amount of beam displacement on each mirror is given as a function of the amount of tilt in one eigenmode or the other. Furthermore, the amount of cavity axis displacement a and cavity axis tilt α is also calculated for each eigenmode using the geometric relationship between a set of mirror tilts and their cavity axis as derived in Appendix 10.1. Figure 6-3 illustrates a cavity in each of the two eigenmodes when using the parameters from Table 6-1.
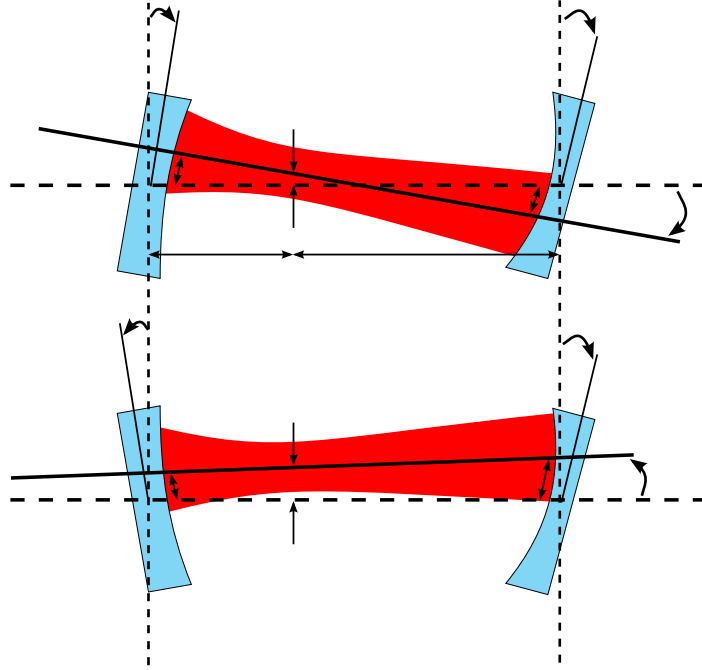
Figure 6-3. Illustration of the orthogonal modes of cavity tilt. The upper diagram shows tilts given by eigenvector $\vec{v}_b$ and the lower diagram shows $\vec{v}_a$. Labels.

6.2.2   Soft and hard modes

The torque to angle transfer function of each of these eigenmodes has the same form as that of a single pendulum (Eq. 6.1.4), but the spring constant is modified. More importantly, the spring constant is modified differently for each mode, yielding distinct behaviors of the two eigenmodes. In this section, we analyze these behaviors and accordingly introduce the names *soft* and *hard* to use in place of *a* and *b* for describing the two modes.

Just as in Sec. 6.1.1, we can take the Laplace transform of each of the equations in Eq. 6.2.13 to get the general form of the modal torque to angle transfer function:

$$H'(s) = \frac{\Theta'(s)}{\tau'_{ext}(s)} = \frac{1}{Is^2 + \gamma s + \kappa_p + \kappa_{rp}}.$$ (6.2.15)

Figure 6-4 shows the control theory view of the addition of the radiation pressure spring constant to the transfer function.
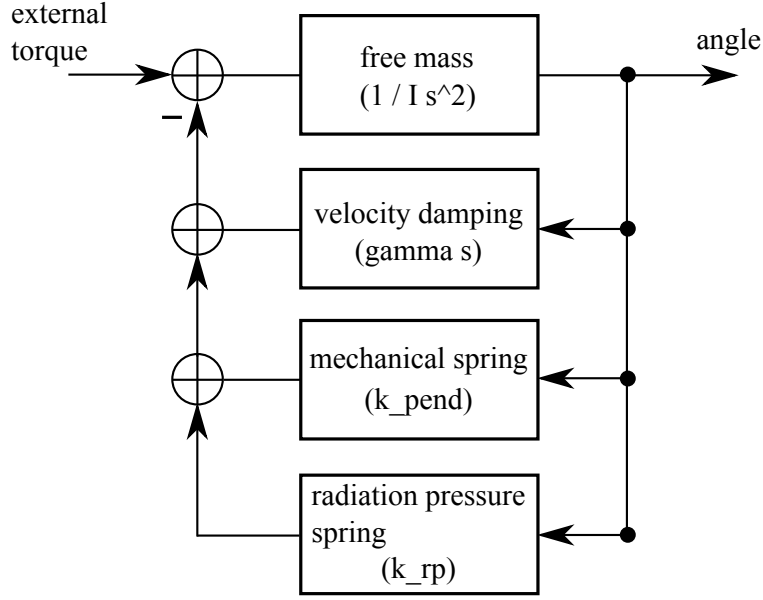
Figure 6-4. Demonstration of how radiation pressure modifies the torque to angle transfer function of a Fabry-Pérot cavity's eigenmodes.

The magnitude and sign of the total torsional spring constant, $\kappa_{tot} = \kappa_p + \kappa_{rp}$, conveys critical information about the stability of the cavity and the nature of its response to external torque. Recalling the equation of an angular spring, $\tau = -\kappa_{tot}\theta$, a restoring torque is provided only if $\kappa_{tot} > 0$, which is equivalent to the condition for stability. If $\kappa_{tot} < 0$, the spring is an anti-spring, resulting in an unstable, run-away situation. Furthermore, while κ_{tot} is positive, its magnitude directly relates to the stiffness of the spring.

The stability criteria for the coupled cavity eigenmodes depend on the relationship between κ_p and κ_{rp}:

$$\text{stable: } k_{tot} > 0 \implies \frac{2PL}{c(1 - g_1 g_2)}\lambda < \kappa_p \tag{6.2.16}$$

$$\text{unstable: } k_{tot} < 0 \implies \frac{2PL}{c(1 - g_1 g_2)}\lambda > \kappa_p. \tag{6.2.17}$$

The pendulum spring constant, κ_p, is always positive, so we can conclude with certainty that the cavity eigenmode is stable as long as the quantity on the left-hand side of Eq. 6.2.17 is negative. However, if this quantity is positive, then its magnitude compared to κ_p determines stability.
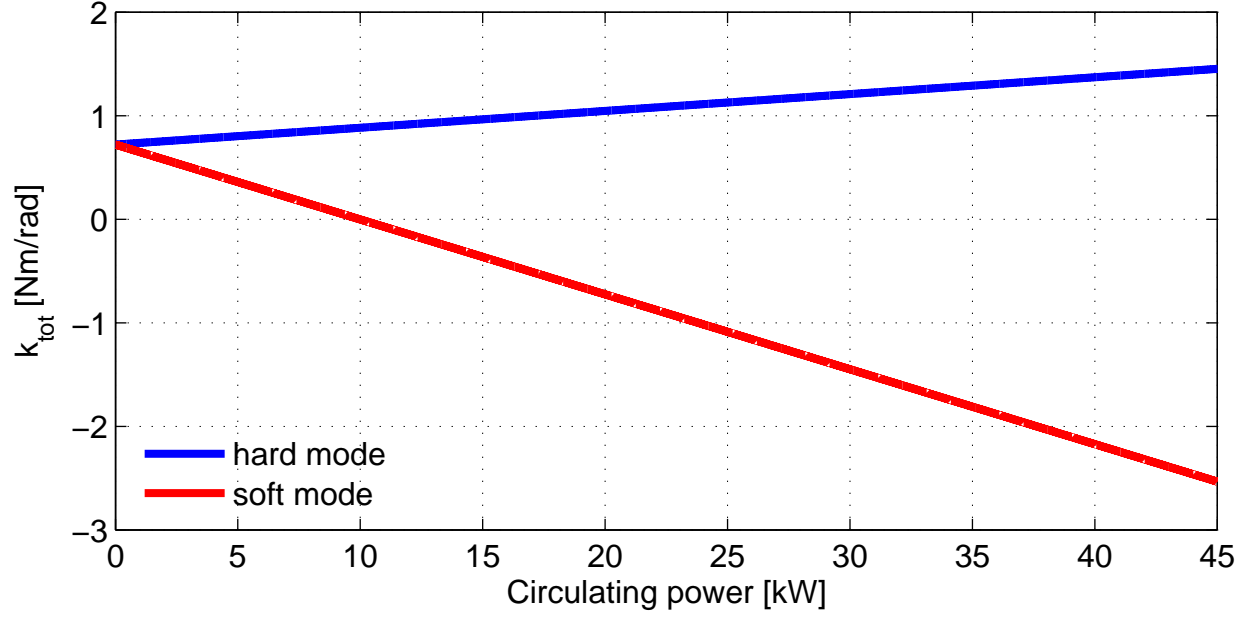
Figure 6-5. Torsional spring constants (pitch) of an optically coupled cavity for LLO parameters. The soft mode is unstable when the spring constant is negative.

Since P, L, and c are all positive numbers and the g-factor is restricted to $0 < g_1 g_2 < 1$ [1] , the sign of the left-hand side is determined solely by that of λ. From the g-parameter restriction, it can be shown that λ_a is always positive and that λ_b is always negative. Therefore, the mode whose mirror angles are described by $\vec{v}_a$ is either stable or unstable, and the mode described by $\vec{v}_b$ will always be stable.

The precise situation for the potentially unstable mode depends on the one non-constant variable, the circulating power P. There is a critical power at which $\kappa_{rp} = -\kappa_p$, and at any greater power, instability ensues. In general, as power increases, the total spring constant for the potentially unstable mode decreases, creating a softer spring, and the total spring constant for the unconditionally stable mode increases, creating a stiffer spring. Thus arise the terms *soft* and *hard* to describe the two eigenmodes that have been referred to by $\vec{v}_a$ and $\vec{v}_b$, respectively.

---

[1] This is the necessary condition for a two mirror resonator to form a stable periodic focusing system. [19, p. 747]

Table 6-2. Torsional spring constants (pitch) for the soft and hard modes of a typical Initial LIGO power and the highest of Enhanced LIGO powers. The soft mode in Enhanced LIGO is unstable. The κ_p values assume a resonant frequency of 0.6 Hz.

	P_{circ}	κ_p	κ_{tot}, soft mode	κ_{tot}, hard mode
Initial LIGO	9 kW	0.721 Nm/rad	0.0734 Nm/rad	0.867 Nm/rad
Enhanced LIGO	40 kW	0.721 Nm/rad	-2.18 Nm/rad	1.38 Nm/rad

Figure 6-5 shows the dependence of κ_{tot} on circulating power for the soft and hard modes of a LIGO arm cavity. Without power in the cavity, the modes are identical and their spring constants are simply that of the individual pendula. The symmetry-breaking effect of radiation pressure comes into play as soon as light resonates in the cavity: the hard mode's spring constant increases and the soft mode's spring constant decreases. The critical power at which the soft mode becomes unstable is 10 kW, which corresponds to approximately 6 W input power (for Enhanced LIGO efficiencies) to the interferometer. Above the critical power, radiation pressure creates an optical anti-spring.

Table 6-2 highlights the values of the spring constants for the typical power that was used in Initial LIGO (9 kW) and for the highest of powers achieved in Enhanced LIGO (40 kW). The corresponding transfer functions for these spring constants is found in Fig. 6-6. The resonant frequency, $\omega_0 = \sqrt{\kappa_{tot}/I}$, increases with power for the hard modes and decreases for the soft modes. Once κ_{tot} becomes negative, as is the case for the Enhanced LIGO soft mode, there is no real resonant frequency.

One final comment about the analysis of the modified transfer function (Eq. 6.2.15) is that the two poles,

$$s = s_\pm = \frac{-\gamma \pm \sqrt{\gamma^2 - 4I\kappa_{tot}}}{2I}, \tag{6.2.18}$$

provide an additional (find better word) way to view the stability of the system. As long as the poles are negative, the impulse response will decay or be sinusoidal. However, if a pole is positive, the system's motion will experience exponential growth. The constraints for $s_\pm$ to be in a particular half of the s-plane are easily derived from Eq. 6.2.18. Note that s_- will always be in the left half of the plane and that s_+ is the pole that has the potential of falling in the right half
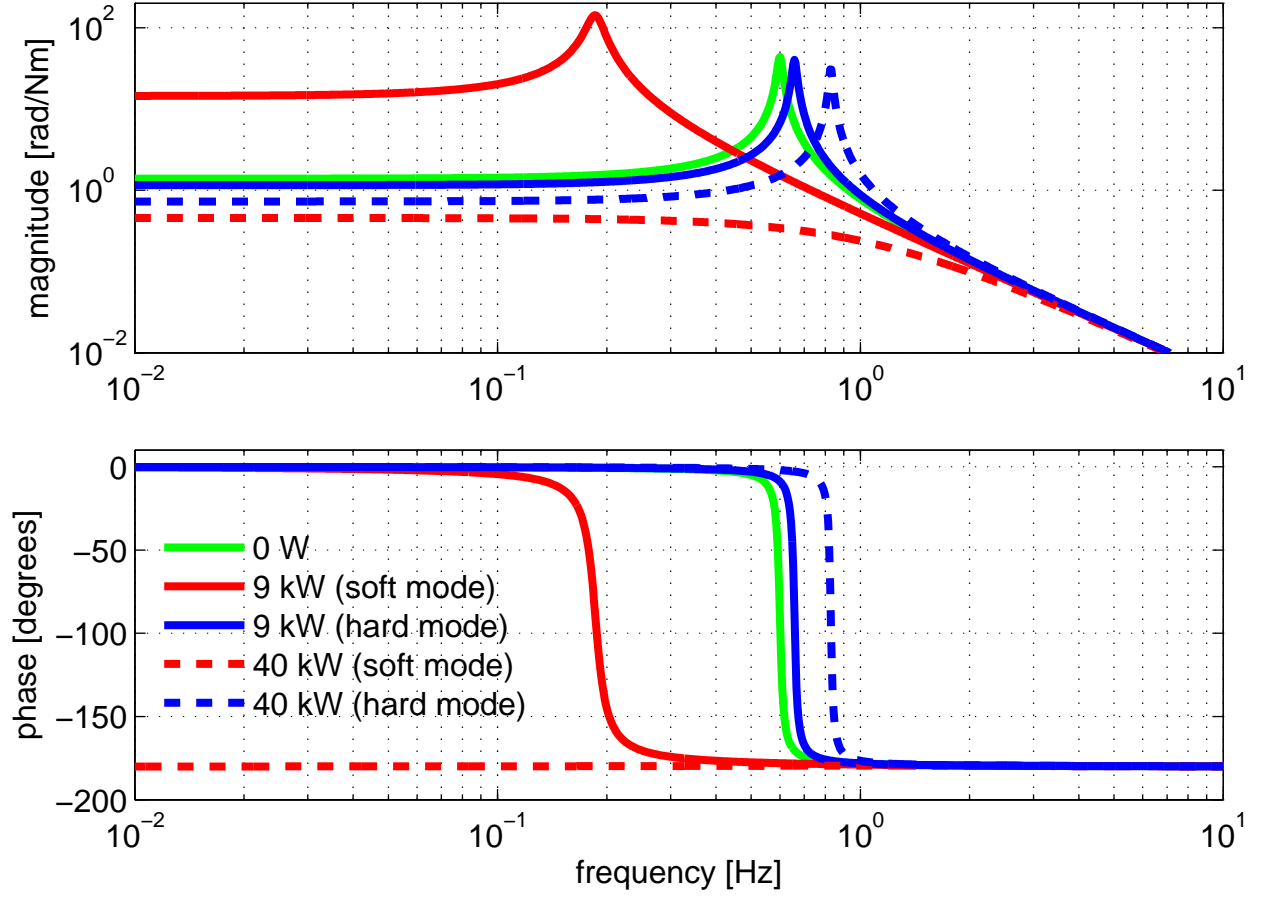
Figure 6-6. Single cavity opto-mechanical transfer function for pitch. The resonant frequency increases with power for the hard mode, but decreases for the soft mode, eventually becoming imaginary. $P_{circ} = 9$ kW (5.25 W input) was a typical operating power for Initial LIGO and $P_{circ} = 40$ kW (23.5 W input) is the highest of powers reached for Enhanced LIGO.

Table 6-3. Conditions on total torsional constant κ_{tot} for determining system stability.

κ_{tot} condition	pole s_+	impulse response
$\kappa_{tot} < 0$	real positive	statically unstable
$\kappa_{tot} = 0$	zero	
$0 < \kappa_{tot} < \gamma^2/4I$	real negative	stable decay
$\kappa_{tot} > \gamma^2/4I$	real negative, and imaginary	stable, oscillatory

of the plane. Table 6-3 show how the s-plane locations for s_+ depend on κ_{tot}. The sign of κ_{tot} determines stability, as expected, and we see that the nature of the stable response depends on the damping coefficient. Figure 6-7 plots the pole locations for a range of κ_{tot} experienced while powering up Enhanced LIGO.

Figure 6-7. Poles of the torque to pitch transfer function as a function of torsional constant, κ_{tot}. Crosses show s_+ and asterisks show s_-. Poles in the right half of the s-plane indicate the system is unstable.

6.3 Implications

These are the transfer functions for which controls must be designed.

6.4 ASC loops

6.4.1 Optical lever servo compensation

CHAPTER 7
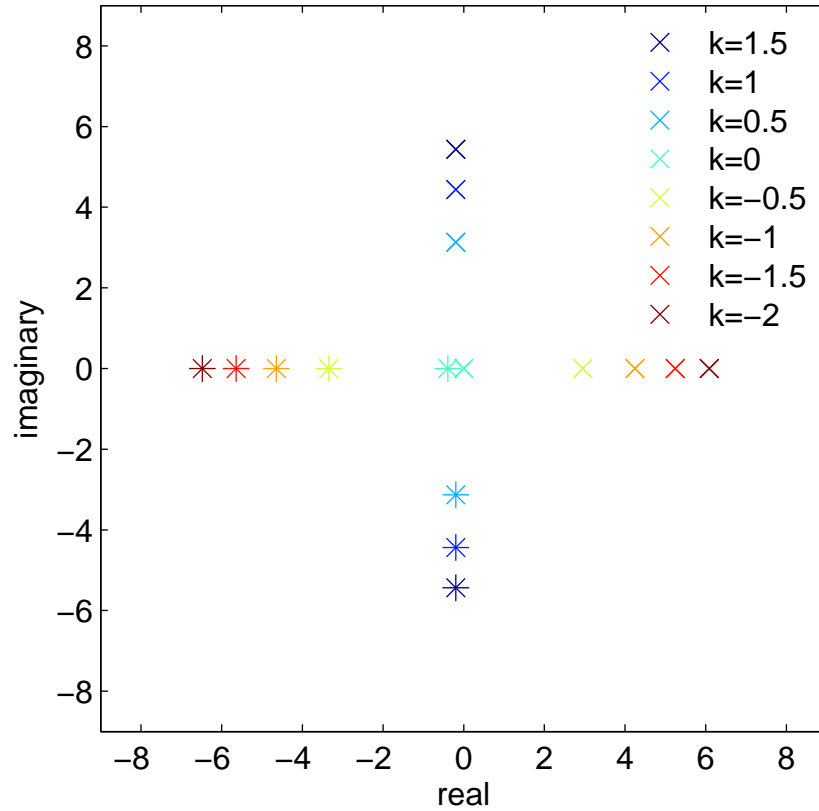# ANGULAR SENSING AND CONTROL CHARACTERIZATION AND PERFORMANCE IN THE RADIATION PRESSURE EIGENBASIS

The basis for angular control in Initial LIGO was the sensor basis. The wavefront sensors are located such that they sense common/differential ETM/ITM angular motion and the filters were designed to feed back to those sets of motions. This does not, however, lend itself to easily handling radiation pressure torque. Since the WFS basis is not the radiation pressure eigenbasis of Section 6.2.1, each control servo handled combinations of the soft and hard modes. Due to radiation pressure, each mirror has two resonances, a more complicated plant than that offered by the eigenbasis which has a single resonance for each mode.

Since the soft mode is statically unstable, it needs high (how high?) DC gain at all times. In the WFS sensor basis, that would mean uniformly increasing the gains of all of the control loops, since the control of the soft mode is split amongst the loops. The problem is that some of the WFS sensors are less good than others, so a uniform gain increase would impress extra sensing noise from all WFS on DARM.

This poses a problem because increasing the gains impresses sensing noise on the mirrors, affecting DARM, and impresses input beam motion on the mirrors, making the interferometer less steady as a whole.

The meat of the Enhanced LIGO ASC upgrade was to switch the control servo from the sensor basis to the natural radiation pressure eigenmode basis, and to keep the contamination to DARM at a minimum.

7.1 Calibrations

Since the data is collected digitally, the units are in digital counts. This must be converted into physical units in order to make meaningful statements beyond relative comparisons. Two ways to make a calibration are to (think about this more!)

- work backwards through the control system and electronics chain
- inject an analog signal with a known amplitude

I describe here the calibrations I made of some of the angular sensing channels, all the while demonstrating particular examples of these methods.

7.1.1 Beam spot motion

A quantity of interest is how much the beam moves on the ITMs and ETMs. It is this beam spot motion which, together with the mirror angular motion, creates a length signal that contributes noise to DARM. An elegant way of following the motion of the beam on the test masses is to track pickoffs of the light transmitted or reflected from the mirrors. We have such signals naturally available for the ETMs and ITMs from the QPDs which are otherwise used for ASC sensing. For example, QPDX and QPDY see the light transmitted through each of the ETMs and WFS2 sees the pickoff of light from the wedge of ITMX.

To calibrate the counts of the QPD and WFS2 pitch and yaw error signals, `L1:ASC-QPDY_{PIT,YAW}_IN1` and `L1:ASC-WFS2_{DCPitchMon, DCYawMon}`, I moved the beam a known distance on the test mass, Δx, and recorded the corresponding Δy of the QPD and WFS2 readback. The ratio $\Delta x/\Delta y$ is the calibration from counts to meters. The details of the procedure are described below.

7.1.1.1 Moving the beam

Moving the beam on the mirrors is straightforward because of the ASC system. All that we need to do is introduce an offset to the setpoint of the of the beam centering aspect of the ASC servo. For the ETMs we put a DC offset in the `L1:ASC-QPD{X,Y}_{PIT, YAW}_{OFFSET}` channel and for the ITMs we changed the X and Y targets of the beam splitter beam centering servo.

7.1.1.2 Measuring how much the beam has moved

The more difficult task is measuring just how much the beam has moved. For this, we make use of the lever arm mechanism of angle to length coupling. (This should be explained in the previous chapter, so maybe just reference it.) The idea is that when the axis of rotation of a mirror coincides with the center of the beam, any tilt of the mirror about this axis does not affect the path length of the reflected beam. However, if there is a mismatch between rotation axis and
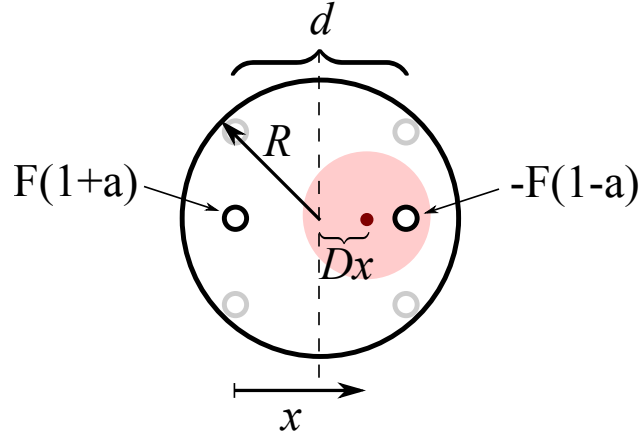
Figure 7-1. Geometry of osems and mirror as used for calculating the location of the axis of rotation when the torques are unequal. Need latex in inkscape!

beam location, then the light will pick up a longitudinal phase shift when the mirror is tilted. During a full interferometer lock, this is recorded by DARM.

The concept of the measurement is to move the axis of rotation of the mirror so that it passes through the center of the beam. We use the OSEMs to change the location of the axis of rotation, and we use DARM to determine when the axis is aligned with the beam center. For example, if we drive the top two osems more than the bottom two osems, we've created an axis of rotation that sits below the center of mass. The result of such tuning is an effective rebalance of the center of mass of the mirror so that it is aligned with the center of the beam. The procedure is:

1. Shake the mirror at some frequency f (we use 39.5 Hz) during a full lock
2. Demodulate DARM at f for several different sets of osem gains
3. Fit a quadratic to the demodulated data to pinpoint the osem gains that minimize the coupling to DARM

Relating the osem gains to absolute beam position on the mirror requires only the geometry of the mirror and osem setup as sketched in Fig. 7-1. We estimate the osem locations as being on the edge of the mirror such that the length d of one side of the square that they form is given by $d = \sqrt{2}R$, where $R = 12.5$ cm is the radius of the mirror. Then, collapsing the four osems into a representative two at the centers of two opposite sides of the square and assigning them gains of $1 + \alpha$ and $-(1 - \alpha)$ for a force F, we can evaluate where the pivot point x is located by setting

	ETMX	ETMY	ITMs
pitch	1.03e-5 m/ct	1.21e-5 m/ct	5.52e-2 m/ct
yaw	0.88e-5 m/ct	0.80e-5 m/ct	4.79e-2 m/ct

Table 7-1. Calibrations to be used with the QPDX, QPDY, and WFS2 DC pitch and yaw error signals for a measure of beam spot motion.

the sum of the torques equal to zero:

$$F[1+\alpha]x = F[1-\alpha][d-x].$$ (7.1.1)

Therefore, the beam location relative to center, Δx, is

$$\Delta x := \frac{d}{2} - x = \alpha\frac{d}{2},$$ (7.1.2)

and for a change in a pitch or yaw coil gain, the change in beam position, Δx, is:

$$|\Delta x| = \frac{|\Delta\text{gain}|R}{\sqrt{2}}.$$ (7.1.3)

The final calibrations of these channels are shown in Table 7-1. [1]

7.1.2   Angular mirror motion

The optical levers provide a straightfoward measure of individual mirror motion. The channels I calibrated were of the form L1:SUS-ETMX_OPLEV_{P,Y}ERROR, the optical lever error signals for each of the large optics. I made use of the dependence of power in a misaligned cavity to calibrate the ETM and ITM optical levers, and used a less precise, rudimentary method to calibrate the RM, BS, and MMT3 optical levers.

7.1.2.1   ETM and ITM optical levers

I calibrated the arm cavity optical levers by tracking the power loss in the locked arm as one of its mirrors is tilted. The closed form expression for cavity power as a function of mirror tilt is

---

[1] A minor technicality is that since there are no filters between the QPD error signals and the offset channel, their units are exactly the same. Thus, calculating meters of beam spot motion as a function of offset serves to calibrate the error point. For convenience, this is what I did.

derived in Appendix 10.2. All that is needed is a quadratic fit to the data collected. From the fit parameters, I can determine the factor, $\Delta\theta/\Delta y$, which converts the digital counts of the optical lever channel, y, to units of radians.

To make the measurement, I locked a single arm and maximized the power build up. Then I slowly stepped the pitch or yaw pointing of one of the mirrors away to one side of resonance, and then back and to the other side, repeating this several times. All the while, I recorded the optical lever error signal of the mirror whose angle I was changing, and the power in the arm as determined from `L1:LSC-NPTR{X,Y}_OUT16`, the amount of light transmitted through the ETMs.

From Eq. 10.2.28, we see that the power in the arm, P, is a function of the form

$$P = P_{max} \exp\left[-b(y - y_0)^2\right], \tag{7.1.4}$$

where b is related to physical cavity axis displacement a and tilt α by $by^2 = (a/w_0)^2 + (\alpha/\theta_0)^2$. In order to relate the optical lever signal, y, to physical cavity parameters, we divide by $\Delta\theta^2$ and rearrange to get:

$$\frac{\Delta\theta}{\Delta y} = \sqrt{b}\left[\left[\frac{\Delta a/\Delta\theta}{w_0}\right]^2 + \left[\frac{\Delta\alpha/\Delta\theta}{\theta_0}\right]^2\right]^{-\frac{1}{2}}. \tag{7.1.5}$$

The terms in the numerators on the right hand side are fixed constants based on the cavity geometry and can be calculated using Eq. 10.1.4. The measurement data and fits are shown for both pitch and yaw in Fig. 7-2. The ETM optical levers make use of a broader range of optical lever signal than do the ITMs. (Also note that the maximum power in the y-arm is about 10% less than that in the x-arm. This is true at both Hanford and Livingston, and is due to the priority given to the x-arm in the alignment scheme, as explained in Appendix 10.3.)

7.1.2.2 RM, BS, and MMT3 optical levers

To calibrate the RM, BS and MMT3 optical levers, I used my own eyes and the camera images and known dimensions of the ETM beam cages. With the interferometer unlocked for the BS and MMT3 calibrations, and the power recycled Michelson locked for the RM calibration, I moved the optics in pitch and yaw, tracking the beam's movement on the ETM cages. For yaw, I moved the mirrors until the beam was centered on each vertical suspension post, and for pitch I
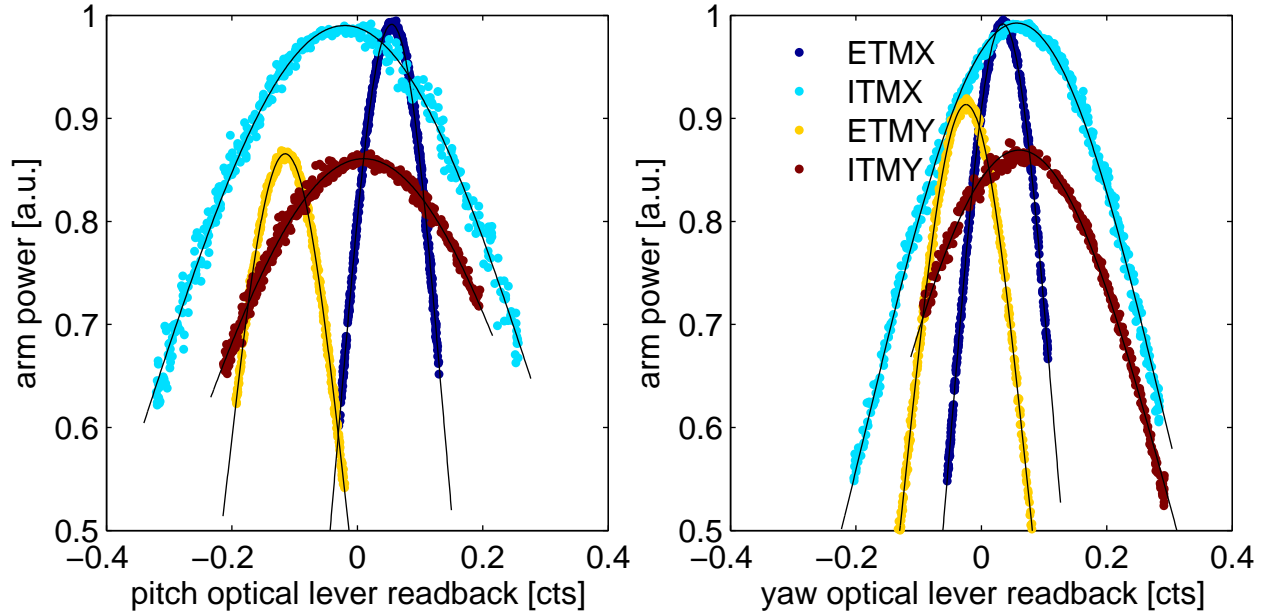
Figure 7-2. Optical lever calibration data and fits to Eq. 7.1.4.

Table 7-2. Calibrations to be used with the optical lever error signals for a measure of angular
mirror motion. Units are µrad/ct.

	ETMX	ETMY	ITMX	ITMY	RM	BS	MMT3
pitch	49.4	43.0	14.9	15.6	61.9	47.3	57.4
yaw	50.7	43.3	20.1	20.2	42.5	63.5	55.5

moved the beam from the center of the mirror to the top of the cage. Small angle approximations
and geometry are the only tools needed to relate beam displacement to mirror angle.

The final $\Delta\theta/\Delta x$ calibrations of all optical levers are in Table 7-2.

7.1.3 WFS error signals

The WFS error signals are physically Watts of power at the detectors. Converting the digital
counts to Watts requires working backwards through the electronics, and can be divided into
two parts. First, we must calibrate the WFS demodulation chain to backtrack WFS counts into
voltage of signal at the input to the mixer. Second, we must convert voltage at the mixer into
Watts at the sensor based on properties of the photodetector RF electronics.

	q1	q2	q3	q4	average
WFS1	0.35	0.32	0.34	0.35	0.34
WFS2	8.8	8.6	8.7	8.5	8.7
WFS3	6.4	5.8	5.8	5.7	5.9
WFS4	6.3	5.4	5.3	7.4	6.1

Table 7-3. Demodulation chain calibration for each quadrant of each WFS. Units are µV/count.

Figure 7-3. LISO model of the 25 MHz resonant RF WFS front end electronics.

7.1.3.1 Counts to Volts

I used an HP signal generator to create an RF sine wave at 100 Hz away from the local oscillator frequency and put this into each quadrant of the demod boards. Comparing the peak to peak voltage of this input sine wave to the peak to peak amplitude in counts as recorded by a dtt time series gives the Volts per count conversion.

For efficiency purposes in making the measurement, we put the output of the HP into an RF splitter so that we could inject a signal into 2 quadrants at once. For WFS1 and WFS2, I dialed the frequency to 24.48433100 MHz with an amplitude of -30 dBm. With an oscilloscope, I measured each output of the RF splitter to have 13.6 mV peak to peak. For WFS3 and WFS4, I used a frequency of 61.21097360 MHz and amplitude of -30 dBm, which read out after the splitter as a 14 mV peak to peak. The calibrations are presented in Table 7-3.

It should be noted that the demod chain calibration numbers for all quadrants of a particular WFS are about the same, meaning the demodulation chain does not distort the error signals.

7.1.3.2 Volts to Watts

The number of volts of signal created by a certain power on the WFS is determined by the transimpedance (Volts/Amp) and responsivity (Amps/Watt) of the diode. A model of the 25 MHz WFS transimpedance is shown in Fig. 7-3. The responsivity is detailed in Section **??**.

7.2 Optical Gain

The WFS optical gain is a measure of how sensitive wavefront sensors are to mirror motion. We want to know how much power in Watts a WFS detects when a particular mirror, or combination of mirrors, is excited by a certain number of radians. We measure the WFS

optical gain all the time during commissioning, yet under the disguise of the name *sensing matrix*. In practice, the sensing matrix is never calibrated into real units, but we do that here for enlightenment using the calibrations of the previous.

7.2.1 Diagonalizing the ASC drive matrix

7.3 Input beam motion

The beam centering servo only operates up to about 10 mHz, meaning the beam-centering degree of freedom is uncontrolled at higher frequencies. The source of beam de-centering on the mirrors is input beam motion. The HAM seismic isolation tables from which the input optics are suspended have resonant "stack" modes from about 0.8 Hz to 3 Hz. The excess table motion at these frequencies is transmitted to the MMTs.

I measured the impression of the input beam motion on the mirrors by increasing the gain of the common-degree-of-freedom WFS servos (CH, CS, RM) for about 10 minutes. Comparing the amount of angular motion of the mirrors from this time of high common WFS gain to a time with nominal WFS gain and similar seismic motion, we can see the effect directly. Fig. 7-4 shows comparison spectra, demonstrating how there is higher test mass motion around 1 Hz when the common WFS gains are higher.

A more quantitative study of the effects of input beam motion is to measure transfer coefficients between the input beam motion and the mirror angular (or beam spot) motion. During a full interferometer lock I put lines in MMT1, MMT2, and MMT3 at 1.05 Hz, 1.25 Hz, and 0.85 Hz, respectively, selecting excitation amplitudes large enough to appear in the common WFS spectra. I compared the amplitudes of the lines in the MMT spectra with those in the WFS spectra. The counts to counts transfer coefficients are shown in Table 7-4. Since sensing is flat, I use the shape of the WFS loop to extrapolate this transfer coefficient at one frequency to other frequencies. The result is a transfer function useful for making a noisebudget of input beam motion to test mass motion. Selecting a science mode time of typical day-time seismic noise, I made a noisebudget as found in Fig. 7-5.
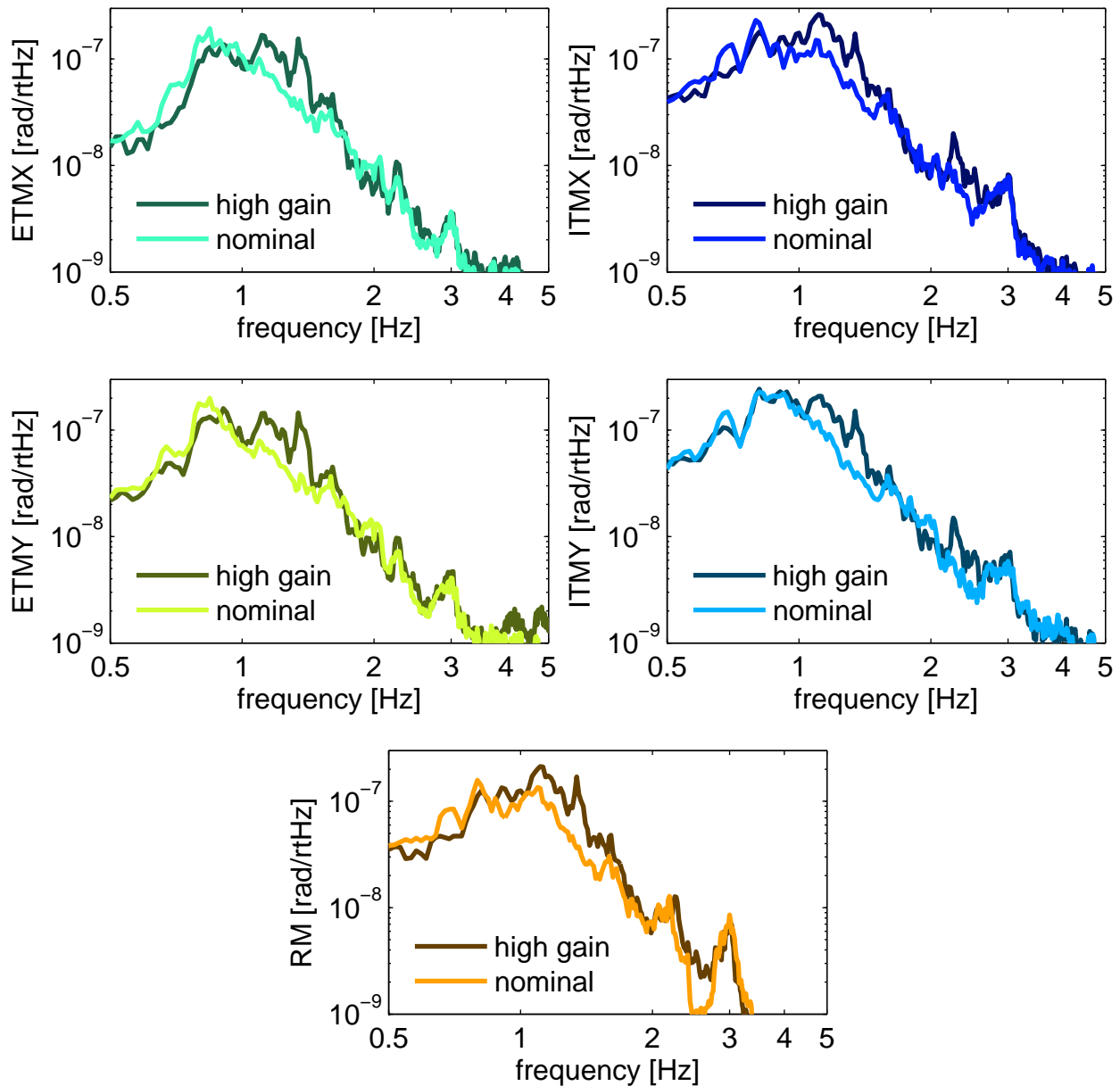
Figure 7-4. Input beam motion impression on the core mirrors. Mirror motion when the common WFS gains (WFS2a, WFS3, WFS4) are increased by a factor of 2.5 is compared to mirror motion when the WFS gains are nominal. Both spectra come from a time of similar seismic activity (typical weekday afternoon noise). But what is the point? The modal WFS spectra simply show more suppression, as expected!

Table 7-4. MMT to WFS transfer coefficients. Make this!!!

Figure 7-5. Noise budget of mirror motion due to input beam impression. Make this!!

7.4   The marginally-stable Power Recycling Cavity

The power recycling cavity (PRC) is the linear cavity formed by the RM and ITMs. Since the radius of curvature of both the RM and the ITMs points in the same direction, the cavity is geometrically unstable. For example, in its cold state at LLO the g-factor of the cavity is 1.00005 and at LHO it's 1.00003. The beam in the PRC is not spatially contained and may be made of many higher order modes. The heating of the ITMs from the kilowatts of power in the arm cavities together with the ITM thermal compensation system (TCS) serve the role of making the PRC geometrically stable for interferometer operation. The heating and cooling of the ITMs is a very complicated process and therefore not very precise, so the value of the hot PRC's g-factor is usually not constant.

The changing g-factor has potentially severe consequences for the ASC. Because of its geometry, the power build-up in the PRC is very sensitve to both the mirror angles and the g-factor. Power fluctuation is detrimental because the signal to noise ratios of the sensors that probe the PRC light degrade due to the presence of increased junk light that contributes shot noise but not signal. WFS1Q, WFS2I, and WFS2Q are the most sensitive to the PRC because their signals are derived from the 25 MHz sidebands. Their sensitivity to mirror motion is therefore subject to change. Since achieving a flat power build-up in the PRC is a difficult task (too much motion in the PRC is quite often a cause of lock loss), we must update the real-time control system to reflect their changing sensitivites. Otherwise, the mirror angles will not be accurately controlled.

An estimate of the expected power fluctuations based on the g-factor and RM motion is a straightforward excercise when using Eq. 10.1.4 and Eq. 10.2.28 as derived in the Appendix. If we estimate the g-factors of the RM and ITM as $g_{RM} = 1 + \delta$ and $g_{ITM} = 1 - \delta$ ($\delta = 6 \times 10^{-4}$ for LLO the cold state) and approximate the distance of each mirror to the cavity waist as z since the two mirrors are very close to each other compared to the waist location, then Eq. 10.1.4 reduces
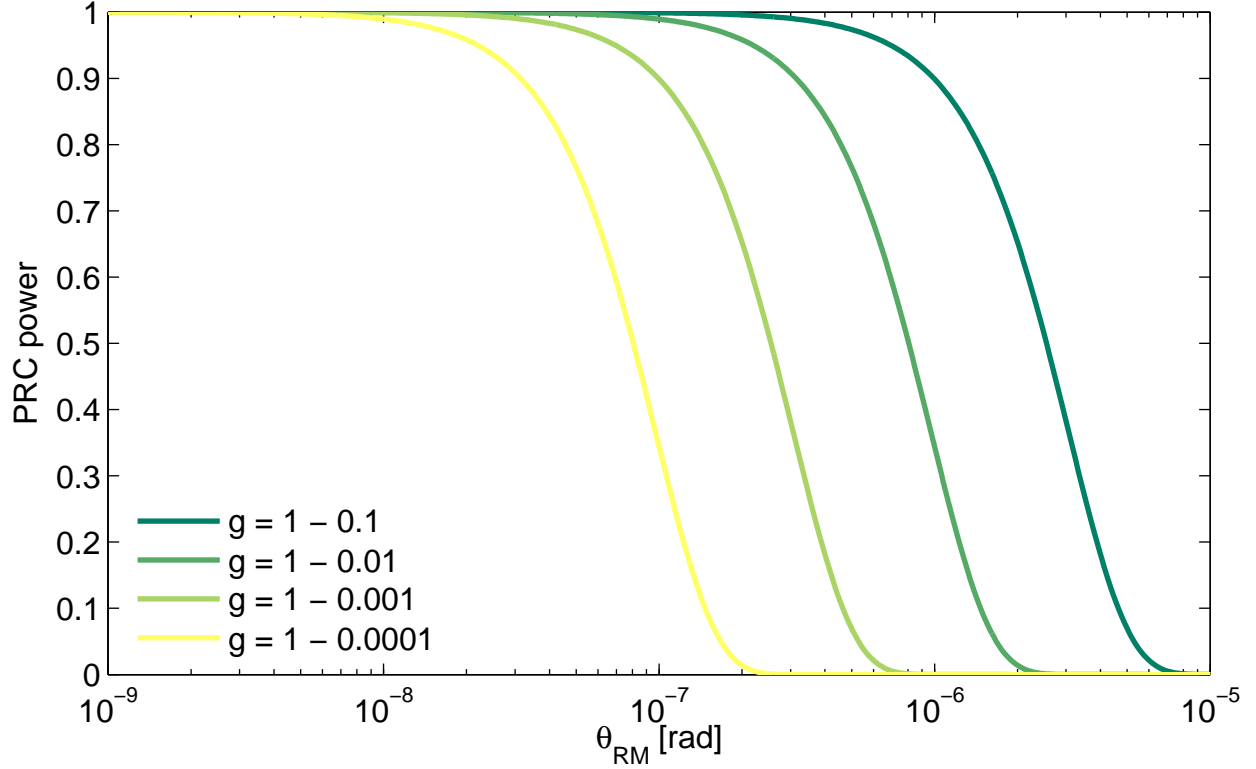
Figure 7-6. Dependence of power build-up in the power recycling cavity on the PRC's *g*-factor and the RM tilt. TCS is necessary for stabilizing the PRC's geometry and therefore its sensitivity to mirror motion. For simplicity, the ITM is assumed stationary in these plots.

to:

$$
\begin{bmatrix} a_{PRC} \\ \alpha_{PRC} \end{bmatrix} = \begin{bmatrix} z(2+\delta)/\delta & z(2-\delta)/\delta \\ -1/\delta & -1/\delta \end{bmatrix} \begin{bmatrix} \theta_{RM} \\ \theta_{ITM} \end{bmatrix}.
\tag{7.4.1}
$$

Fig. 7-6 plots the power in the PRC as a function of θ_{RM} for several values of δ, demonstrating the sensitivity of the PRC to the ITM heating. For example, the typcial RM angular displacement of 10^{-7} rad results in a 66% power loss when the PRC *g*-factor is very near instability with a value of $1 - 0.0001$. Only as the *g*-factor moves further from 1 does the angular motion of the RM have less and less of an effect on the power build-up.

7.4.1 SPOB power scaling

The effect of the marginally stable recycling cavity can be seen by tracking the ASC sensing matrix elements as *g* changes. I excited three of the test masses (ETMX, ITMX, RM) at three

different frequencies (9.7 Hz, 10.7 Hz, and 11.7 Hz, respectively) during a full interferometer lock and changed the TCS settings so that over the course of 15 minutes the *g*-factor steadily changed. Demodulating each of the WFS signals at each of the three excitation frequencies as a function of time shows the strength of the WFS response to the motion of these three mirrors over the course of the study. To compensate for the difference in pendulum responses to the excitations, I multiplied the demodulated signals for a particular excitation f by $(f/9.7)^2$. I also normalized the response by the phase of the mirror's motion as witnessed by the optical levers.

The results are shown in Fig. 7-7. As expected, WFS1Q, WFS2I, and WFS2Q show dependence on the PRC power, and therefore the *g*-factor. The WFS3 and WFS4 sensing elements are flat. The power in the PRC as measured by the $2f$-demodulated POB signal, NSPOB, is also shown in Fig. 7-7 for this time period. In order to compensate for this *g*-factor dependence, we multiply the WFS{1Q, 2I, 2Q} error signals in real-time by

$$\frac{1}{P_{in}} \left[\frac{NSPOB}{350} \right]^{-1/2} \tag{7.4.2}$$

and WFS3I and WFS4I by $1/P_{in}$, where the 350 is the reference NSPOB, treated as nominal. Thus, during interferometer operation, all WFS signals are normalized to input power and are not dependent on the PRC power. This correction to the WFS signals is called SPOB power scaling.

7.4.2 Sideband imbalance

Show OSA scan of AS port.

7.5 DC readout related measurements

- RF created from DC offset beam moving on WFS1

- RF vs DC vs power comparison of (AS) beam spot motion on WFS1

7.6 The effect of the ASC

7.7 ASC to DARM noisebudget
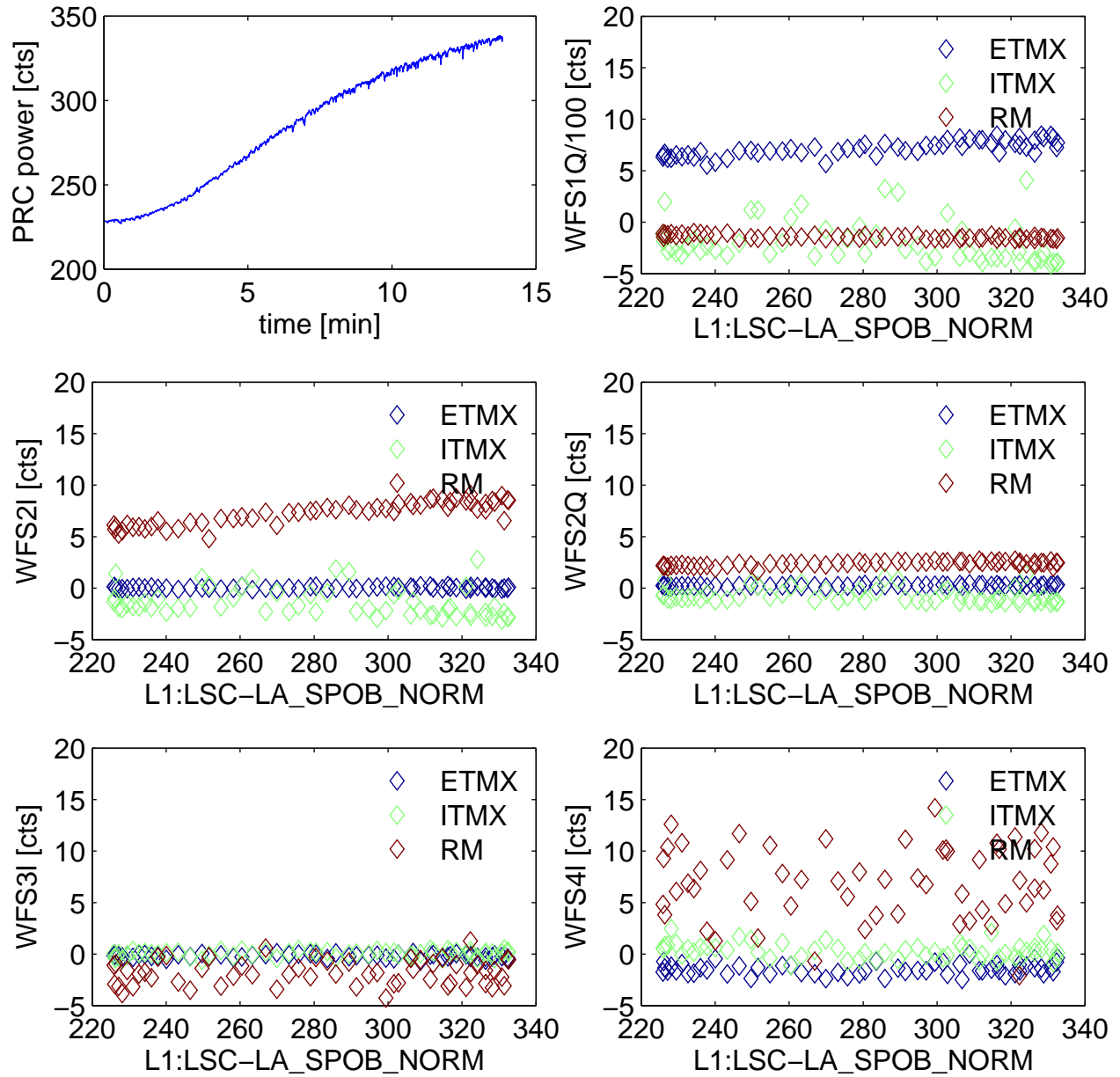
Broadband effect on DARM.

Figure 7-7. Measurement of the dependence of the WFS error signals on the power recycling cavity geometry. WFS1Q, WFS2I, WFS2Q are more sensitive to test mass motion as the power in the recycling cavity increases. To achieve a dependable feedback system, the error signals are scaled in real-time, forcing their responses to be flat with power. This range of SPOB is low for normal operations.
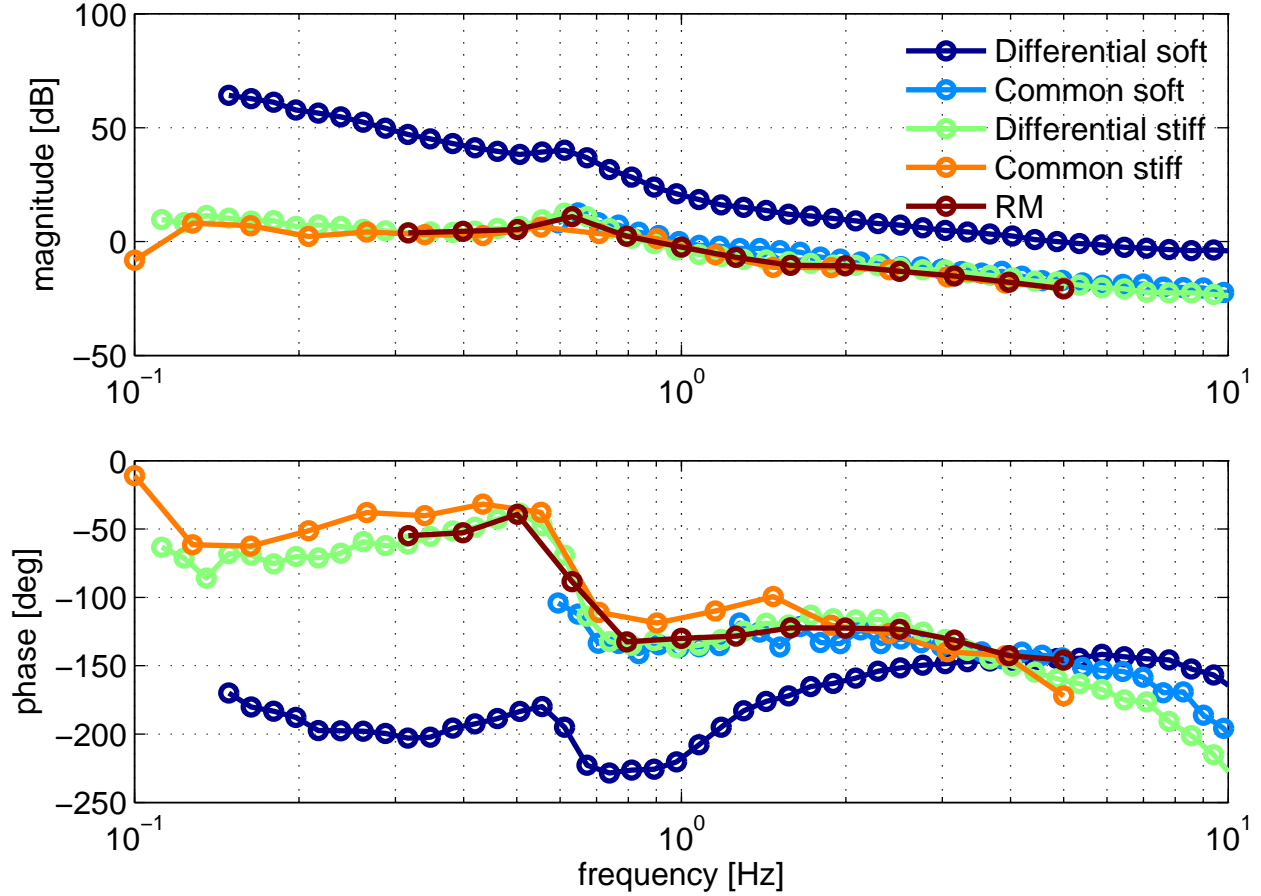
Figure 7-8. Open loop gains (pitch) of the 5 WFS loops as measured with 6 W input power.

7.7.1 Tuning the cut-off filters

The cut-off frequency of the lowpass filters for the WFS control are of particular importance in the DARM noisebudget. The lowpass filter is necessary for suppressing the impression of sensing noise on suspension control.

7.8 Feed-forward

7.9 Advanced LIGO

The Advanced LIGO interferometers will have heavier mirrors, a stable recycling cavity, and more circulating power.
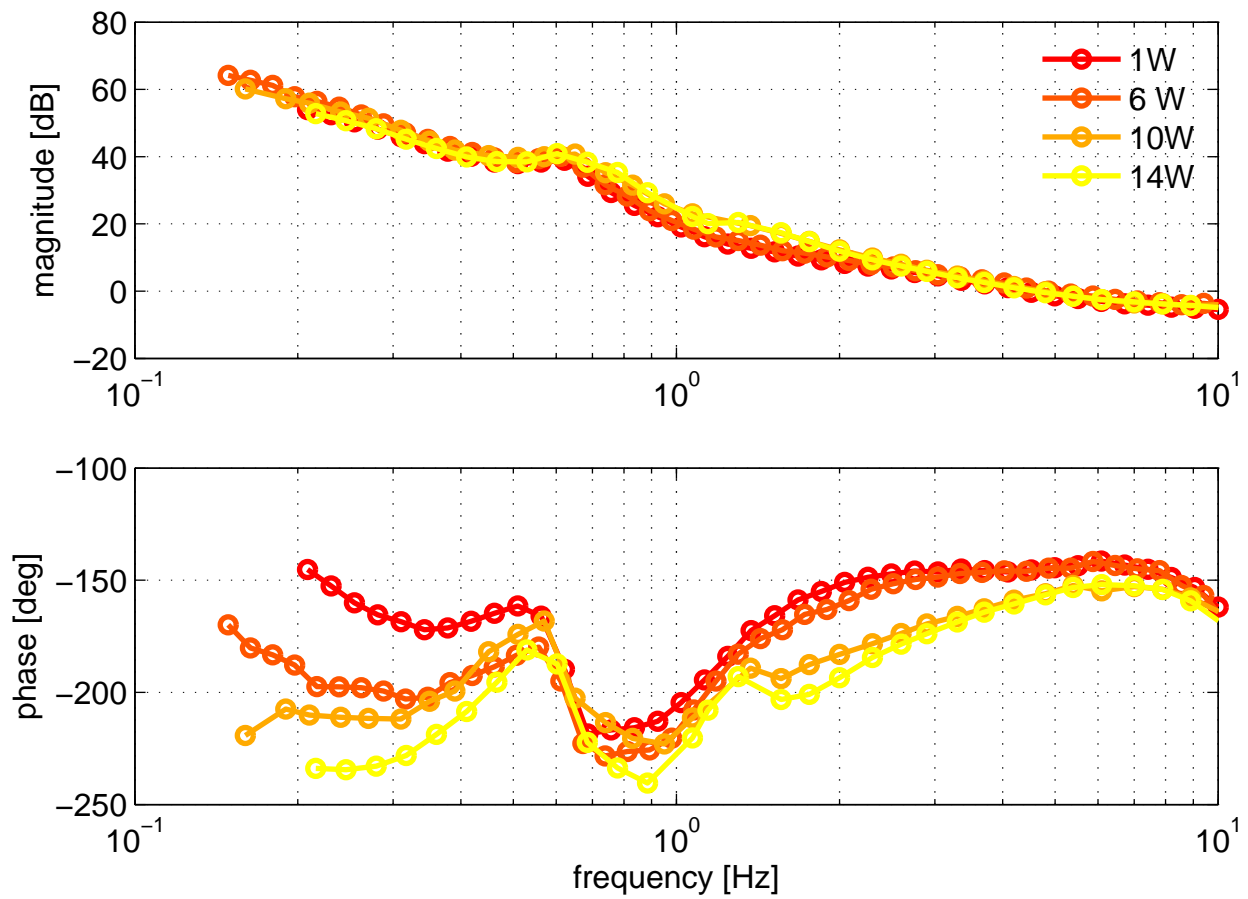
Figure 7-9. Open loop gains (pitch) of the differential soft (WFS1) loop as measured at four
different powers.
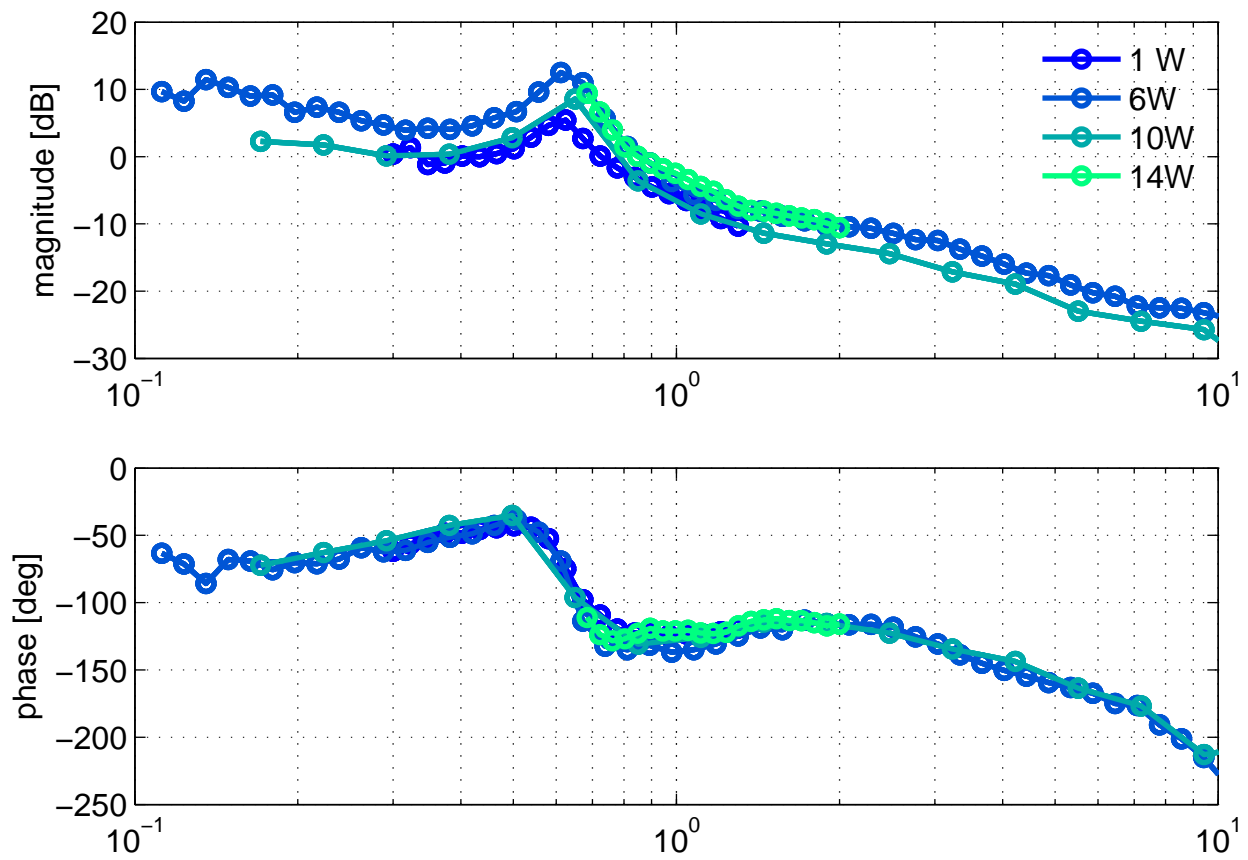
Figure 7-10. Open loop gains (pitch) of the differential hard (WFS2B) loop as measured at four different powers.

Figure 7-11. Propagation of sensor signals from 10 W lock through input matrix and power scaling to eigenbasis, compared with eigenbasis reconstruction of optical lever signals when interferometer not locked, but optics under oplev damping. Data are taken 45 minutes apart. Perhaps include loop-undone backgrounds, too, using my measured OLTFs.
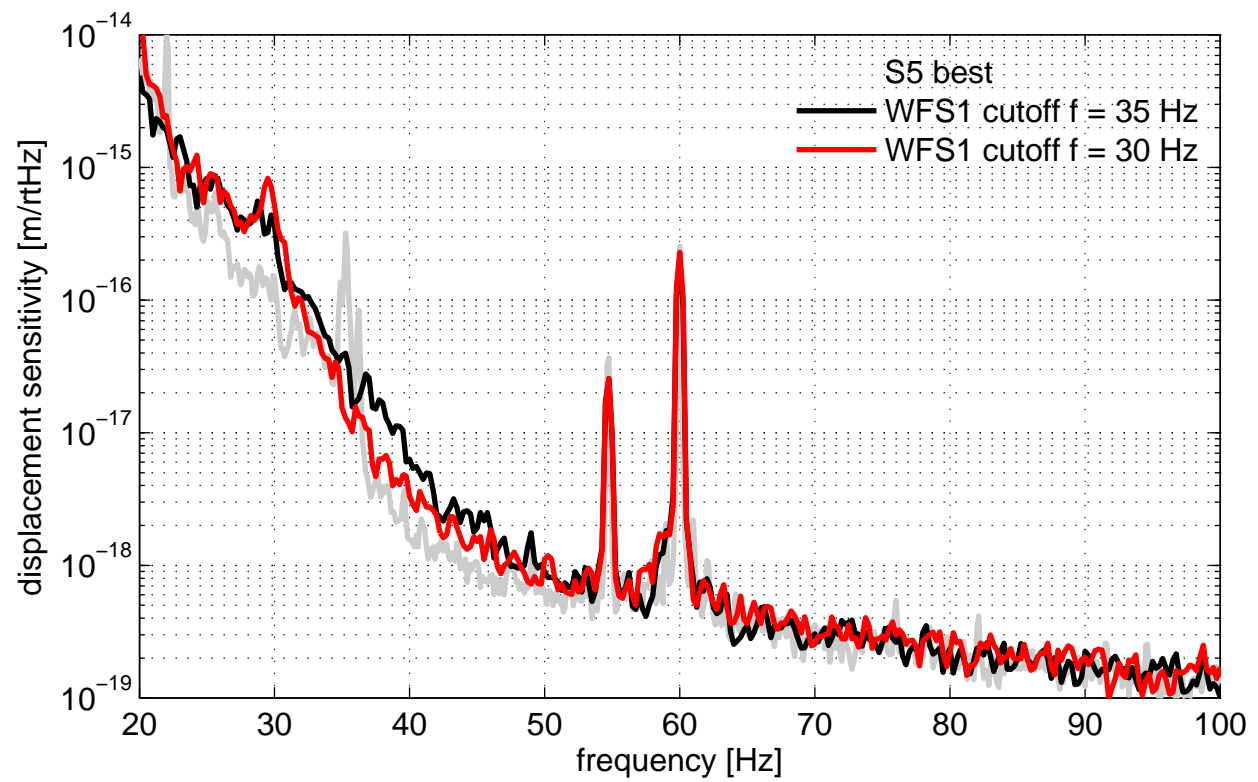
Figure 7-12. Effect of the WFS1 lowpass filter cutoff frequency on strain sensitivity.

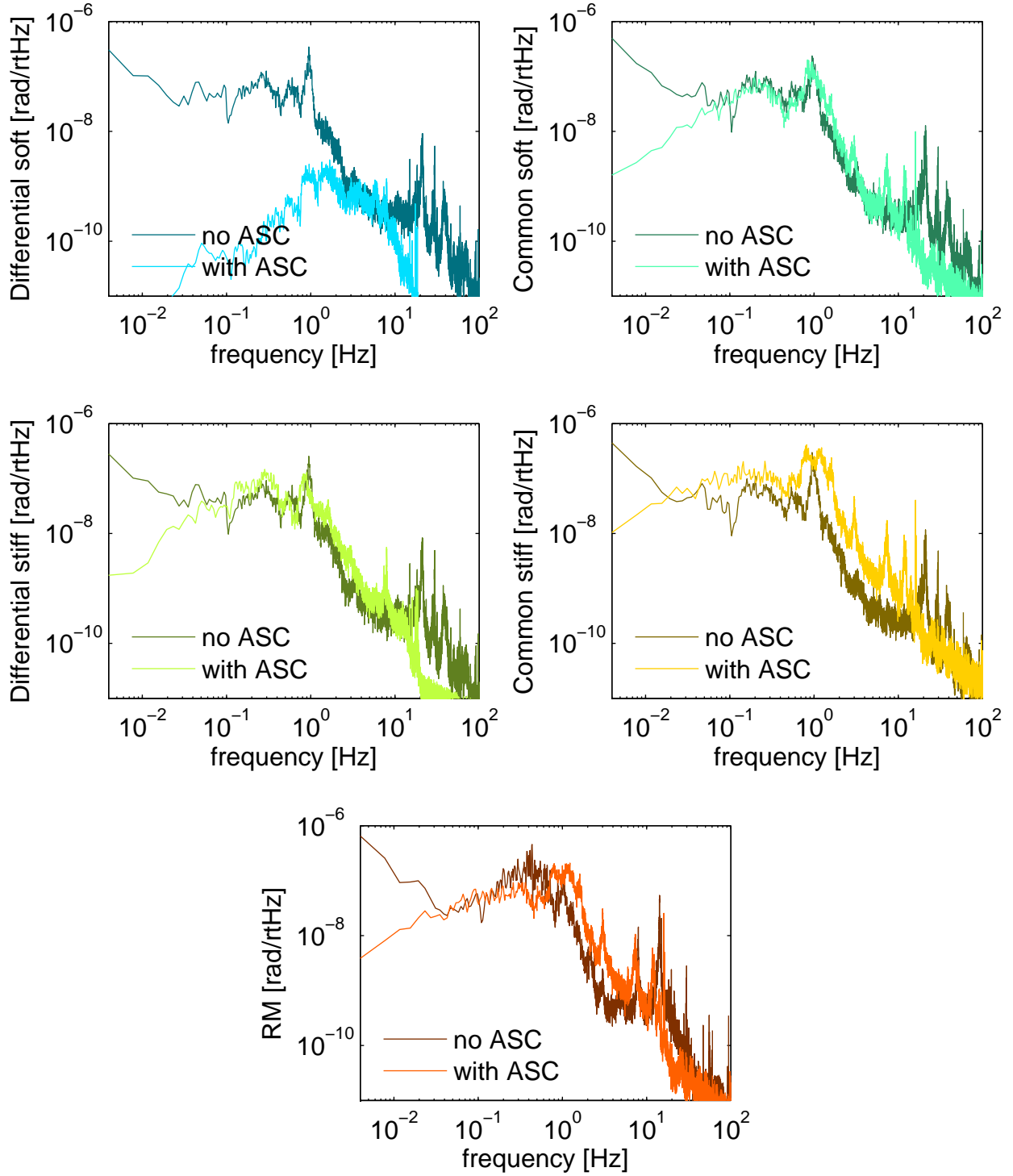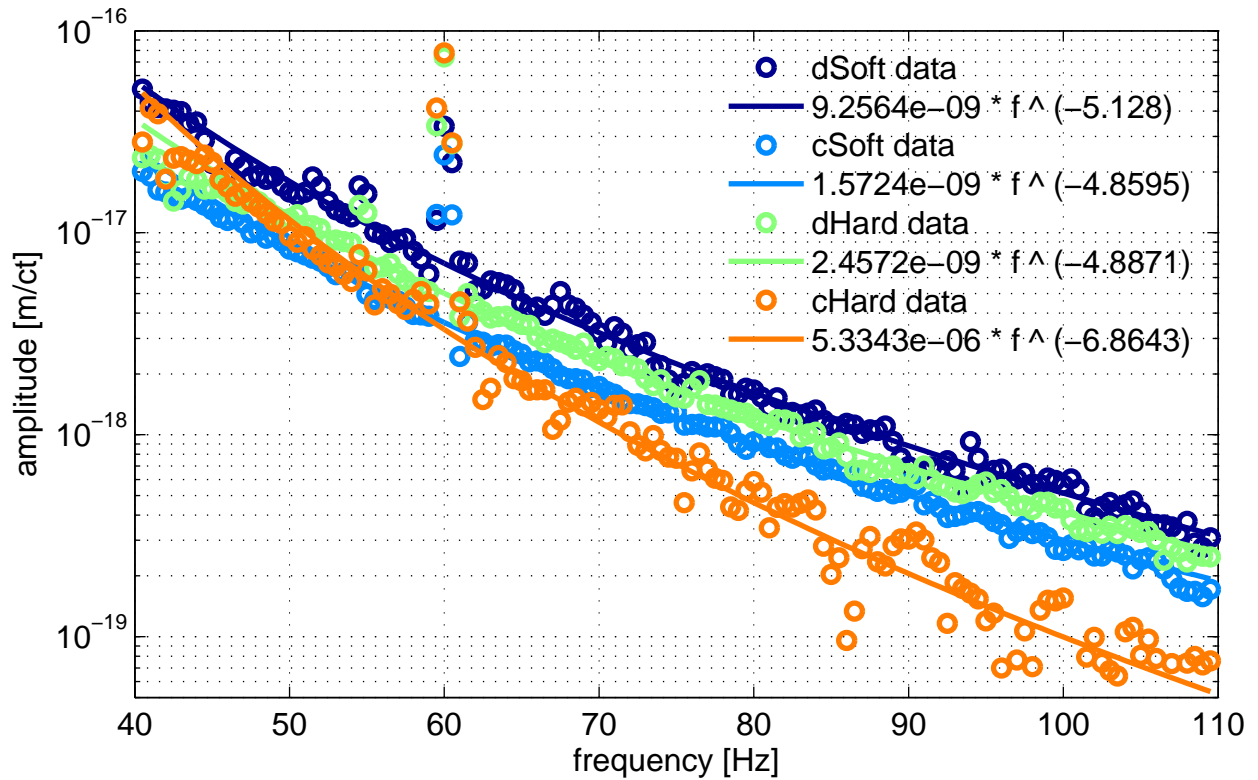Figure 7-13. ASC to DARM transfer function for four of the five wavefront sensor loops. The RM to DARM transfer function could not be measured because the contribution is so small. The fitted curves can be multiplied by the WFS error signals at any time to calculate the ASC noise contribution to DARM. Need to turn cts into Watts.

CHAPTER 8
EXPERIMENTAL MEASUREMENT OF THE SIDLES-SIGG EFFECT

8.1   Measured modes
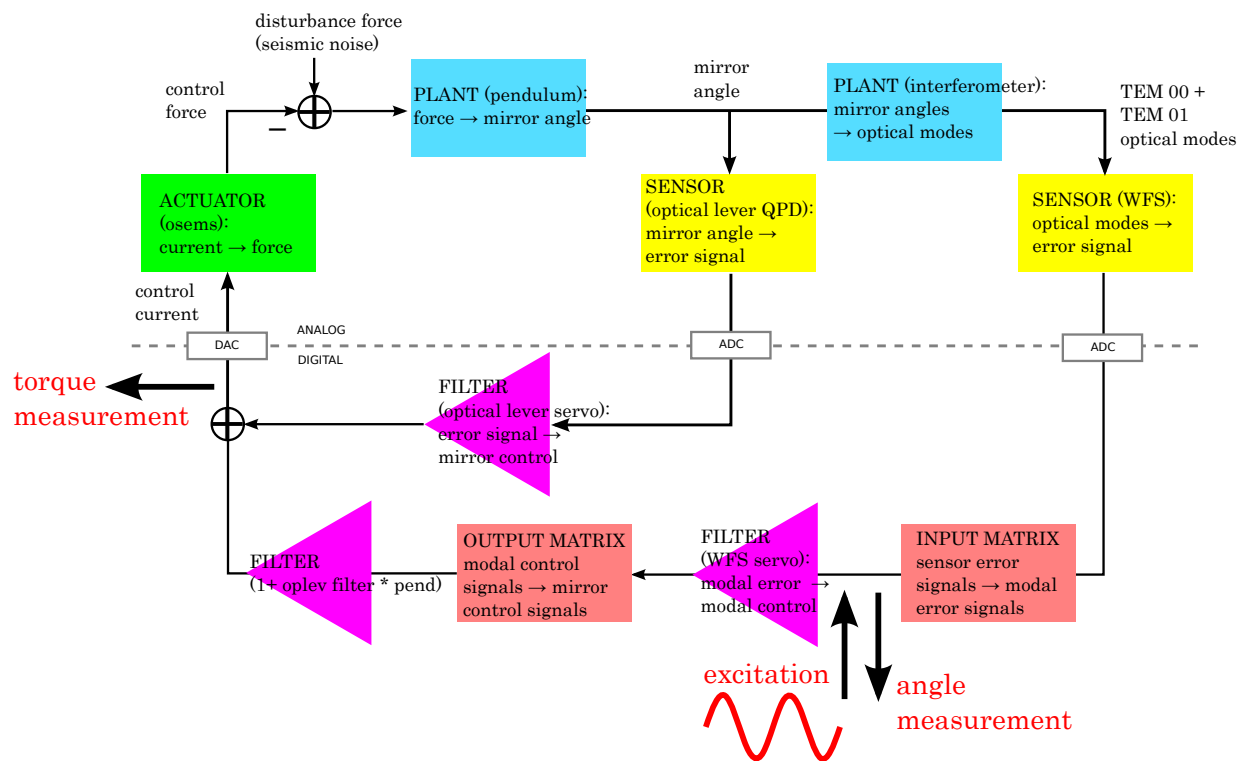
Figure 8-1

CHAPTER 9
SUMMARY

469.75502pt

Figure 9-1. Reflected beam from the Advanced LIGO pre-mode cleaner.

10.1 Misaligned cavity axis

Here I provide the geometric argument that shows how to calculate the tilt a and displacement α of a cavity as a function of mirror misalignment. Cavity tilt is defined by the angle formed between the line that connects the two beam spots (as given by Eq. 6.2.1) and the line joining the centers of the mirrors. Cavity displacement uses the same two lines, yet is defined by the distance between them at the location of the waist of the resonant spatial mode. Based on pure geometry, the cavity displacement and tilt are:

$$\left[\begin{array}{c} a \\ \alpha \end{array}\right] = \frac{1}{L} \left[\begin{array}{cc} z_2 & z_1 \\ -1 & 1 \end{array}\right] \left[\begin{array}{c} x_1 \\ x_2 \end{array}\right] \tag{10.1.1}$$

where z_i is the distance to the waist from mirror i calculated as:

$$z_1 = \frac{g_2(1-g_1)L}{g_1+g_2-2g_1g_2} \tag{10.1.2}$$

$$z_2 = L-z_1. \tag{10.1.3}$$

Clearly, we can combine Eqs. (6.2.1) and (10.1.1) to arrive at an equation directly relating mirror tilt to cavity displacement and tilt:

$$\left[\begin{array}{c} a \\ \alpha \end{array}\right] = \frac{1}{1-g_1g_2} \left[\begin{array}{cc} g_2z_2+z_1 & z_2+g_1z_1 \\ -g_2+1 & -1+g_1 \end{array}\right] \left[\begin{array}{c} \theta_1 \\ \theta_2 \end{array}\right]. \tag{10.1.4}$$

10.2 Power in a misaligned cavity

I'll show how to calculate the power in a cavity as a function of cavity axis displacement and tilt. Combined with the results of Eq. 10.1.4 we determine how the power build-up in a cavity depends on a single mirror's angular displacement.

The field of a lowest-order Gaussian laser beam along one axis at the beam waist is:

$$\psi(x) = U_0(x) = \left[\frac{2}{\pi w_0^2}\right]^{1/4} \exp\left[-\left[\frac{x}{w_0}\right]^2\right] \tag{10.2.1}$$

where w_0 is the beam waist radius and U_0 is the lowest-order Hermite polynomial. The Hermite polynomials are orthonormal, ie. $\langle U_i \mid U_j \rangle = \delta_{ij}$. For example, the next to lowest order polynomial is:

$$U_1(x) = \left(\frac{2}{\pi w_0^2} \right)^{1/4} \frac{2x}{w_0} \exp\left[-(x/w_0)^2 \right] = \frac{2x}{w_0} U_0(x) \tag{10.2.2}$$

10.2.1 Displaced cavity

The field of a cavity with a *displaced* z-axis at the cavity waist is:

$$\psi\prime(x) = \psi(x - a) \tag{10.2.3}$$

$$= U_0(x - a) \tag{10.2.4}$$

$$= c_0 U_0(x) + c_1 U_1(x) + c_2 U_2(x) + \ldots \tag{10.2.5}$$

$$\tag{10.2.6}$$

where a is the displacement of the axis and c_i are constants.

We want to know c_0, the projection of the displaced cavity field onto the beam field:

$$c_0 = \langle \psi \mid \psi\prime \rangle \tag{10.2.7}$$

$$= \int_{-\infty}^{\infty} \psi(x) \psi\prime(x) \, dx \tag{10.2.8}$$

$$= \exp\left[-a^2/2w_0^2 \right] \tag{10.2.9}$$

The power in this mode is the square of the overlap of the two fields:

$$P_0 = |\langle \psi \mid \psi\prime \rangle|^2 \tag{10.2.10}$$

$$= \exp\left[-[a/w_0]^2 \right] \tag{10.2.11}$$

For the purpose of wavefront sensing, we need to know the amplitude, c_1, of the first order U_1 field. This can be approximated as demonstrated in Anderson [20] using the Taylor series expansion of the exponential in $\psi\prime(x) = U_0(x - a)$, assuming a displacement a that's small

compared to waist size w_0.

$$\psi\prime(x) = \left[\frac{2}{\pi w_0^2}\right]^{1/4} \exp\left[-\left[\frac{x-a}{w_0}\right]^2\right] \tag{10.2.12}$$

$$= \left[\frac{2}{\pi w_0^2}\right]^{1/4} \left[1 - \left[\frac{x-a}{w_0}\right]^2 + \mathcal{O}(a^4)\right] \tag{10.2.13}$$

$$= \left[\frac{2}{\pi w_0^2}\right]^{1/4} \left[\frac{2xa}{w_0^2}\left[1 - \frac{x^2}{w_0^2} + ...\right] + \left[1 - \frac{x^2}{w_0^2} + \frac{1}{2}\frac{x^4}{w_0^4} - ...\right] + \mathcal{O}(a^2)\right] \tag{10.2.14}$$

$$= \left[\frac{2}{\pi w_0^2}\right]^{1/4} \left[1 + \frac{2xa}{w_0^2} + \mathcal{O}(a^2)\right] \exp\left[-\left[\frac{x}{w_0}\right]^2\right] \tag{10.2.15}$$

$$= U_0(x) + \frac{a}{w_0}U_1(x) + ... \tag{10.2.16}$$

Notice that here we find $c_0 = 1$, which is consistent with the exact result of Eq. 10.2.9 when we apply our $a^2 \approx 0$ approximation. We find that the amplitude of the first order Hermite-Gauss field for a displaced cavity is

$$c_1 = a/w_0. \tag{10.2.17}$$

10.2.2 Tilted cavity

The field of a cavity with a *tilted* z-axis at the cavity waist is a tad more complex to derive. We assume the tilt, α, is small such that $\sin\alpha \approx \alpha$ and $\cos\alpha \approx 1$. Also, we assume the beam divergence angle, $\theta_0 = \lambda/\pi w_0$, is small such that the wavefronts near the waist can be considered parallel to one another.

Here, the important quantity to consider is the phase of the cavity field at the cross-section of the beam waist. The phase is either advanced or retarded compared to that of the beam:

$$\psi\prime(x) = \psi(x\prime)\exp\left[-ikz\prime\right] \tag{10.2.18}$$

$$\approx \psi(x\cos\alpha)\exp\left[-ikx\sin\alpha\right] \tag{10.2.19}$$

$$\approx \psi(x)\exp\left[-ikx\alpha\right] \tag{10.2.20}$$

$$= U_0(x)\exp\left[-ikx\alpha\right] \tag{10.2.21}$$

where $k = 2\pi/\lambda$ and λ is the wavelength of the laser light.

The overlap of the fields of the beam and tilted cavity is $\exp[-\alpha^2/2\theta_0^2]$. Therefore the power is:

$$P_0 = \exp[-(\alpha/\theta_0)^2].\tag{10.2.22}$$

An expansion of the exponential in Eq. 10.2.21 for a small tilt α gives:

$$\begin{aligned}\psi\prime(x) &= U_0(x)[1 + ikx\alpha + \mathcal{O}(\alpha^2)]\tag{10.2.23}\\ &= U_0(x) + \frac{ik\alpha w_0}{2}U_1(x) + \mathcal{O}(\alpha^2).\tag{10.2.24}\end{aligned}$$

Therefore, the amplitude of the first order Hermite-Gauss field for a tilted cavity is

$$c_1 = ik\alpha w_0/2.\tag{10.2.25}$$

10.2.3 Displaced and tilted cavity

The most general case, of course, is to have a cavity axis that is both displaced *and* tilted at the beam waist:

$$\psi\prime(x) = \psi(x-a)\exp[-ik(x-a)\alpha].\tag{10.2.26}$$

We find:

$$\langle \psi \mid \psi\prime \rangle = \exp\left[-\frac{a^2}{2w_0^2}\right]\exp\left[-\frac{\alpha^2}{2\theta_0^2}\right]\exp\left[-\frac{ia\alpha}{x_0\theta_0}\right]\tag{10.2.27}$$

and

$$P_0 = \exp\left[-\frac{a^2}{w_0^2}\right]\exp\left[-\frac{\alpha^2}{\theta_0^2}\right].\tag{10.2.28}$$

10.3 Initial DC alignment of the interferometer

After any kind of in-vacuum work, the DC alignment of the mirrors is usually too poor for the interferometer to lock. A bootstrapping process of tweaking the alignment by hand is necessary, assuming the mirrors start out pointing in generally the right direction, as is usually the case. As pointed out in 5.1, the QPDs at the end stations are the fixed reference points for the overall alignment, so this process begins with making sure the light reaches them. We then adjust the rest of the mirrors to maximize power build-up in the arms and to maximze spatial overlap of the light reflected from each arm.

An outline of the process is presented here. "Misalign" means to intentionally point a mirror so far away from any known good positions as to eliminate it from the configuration. "Align" and "restore" mean to bring a mirror or configuration to the best known position(s). Centering the beam on a mirror is accomplished by using the suspension cage surrounding the mirror as a reference. Camera images and QPD readback provide the signals used for beam centering.

X-arm
- restore the x-arm (misalign RM, ITMY, and ETMY, align ITMX and ETMX)
- use ITMX to center the beam on QPDX
- use ETMX to center the beam on ITMX
- with x-arm locked, use MMT3 to maximize the x-arm power build-up (NPTRX, can expect about 95%)
- save the MMT3, ITMX, and ETMX alignment settings

Y-arm
- restore the y-arm (misalign ITMX and ETMX, align ITMY and ETMY)
- use ITMY to center the beam on QPDY
- use ETMY to center the beam on ITMY
- with y-arm locked, use BS to maximize the y-arm power build-up (NPTRY, can expect about 90%)
- save the BS, ITMY, and ETMY alignment settings

Relative x-arm and y-arm
- note AS beam position on camera while toggling between x-arm and y-arm locks
- use ETMs to align the two AS beams
- restore the Michelson (misalign ETMs, align ITMs)
- use BS to make AS port as dark as possible
- re-do y-arm alignment if ambitious

Recycling mirror
- restore the PRM (misalign ETMs, align ITMs and RM)
- use RM to center beam on ETMY cage

Restore full interferometer–off you go!

10.4   Channel names

It is often confusing why there are so many channels with almost identical names. And just what those names mean can also sometimes be elusive. The best advice I have to offer about how to figure out for one's self what the root of the channel name conveys about the data it

represents is to browse the MEDM screens. The MEDM screens pictorially show the flow of which channels are derived from others, and whether they sit before or after an excitation point, for example. They also sometimes offer hints as to exactly what calculation is done under the scene in the front-end code to compute new channels.

The topic I want to cover here is the difference between the `OUT`, `OUT16`, `OUTPUT`, and `OUTMON` channel name extenstions. They appear in all of the subsystems, and it is crucial to realize that some are good for analyzing data and some good for getting only a sense in real-time of what's going on. Some are typically recorded to disk, and some are not. These concepts extend to other common name extensions as well.

REFERENCES

[1] S. Solimeno, F. Barone, C. de Lisio, L. Di Fiore, L. Milano, and G. Russo, Physical Review A **43**, 6227 (1991), URL http://dx.doi.org/10.1103/PhysRevA.43.6227.

[2] J. Sidles and D. Sigg, Physics Letters A **354**, 167 (2006), ISSN 03759601, URL http://dx.doi.org/10.1016/j.physleta.2006.01.051.

[3] E. Hirose, K. Kawabe, D. Sigg, R. Adhikari, and P. R. Saulson, Appl. Opt. **49**, 3474 (2010), URL http://dx.doi.org/10.1364/AO.49.003474.

[4] L. Barsotti and M. Evans, Tech. Rep. T080186, LIGO Laboratory (2009), URL https://dcc.ligo.org/cgi-bin/private/DocDB/ShowDocument?docid=6570.

[5] P. Linsay, P. Saulson, R. Weiss, and S. Whitcomb, Tech. Rep. T830001, Massachusetts Institute of Technology (1983).

[6] B. P. Abbott, R. Abbott, R. Adhikari, P. Ajith, B. Allen, G. Allen, R. S. Amin, S. B. Anderson, W. G. Anderson, M. A. Arain, et al., Reports on Progress in Physics **72**, 076901+ (2009), ISSN 0034-4885, URL http://dx.doi.org/10.1088/0034-4885/72/7/076901.

[7] F. Acernese, P. Amico, M. Alshourbagy, F. Antonucci, S. Aoudia, P. Astone, S. Avino, L. Baggio, G. Ballardin, F. Barone, et al., Journal of Optics A: Pure and Applied Optics **10**, 064009+ (2008), ISSN 1464-4258, URL http://dx.doi.org/10.1088/1464-4258/10/6/064009.

[8] H. Lück, M. Hewitson, P. Ajith, B. Allen, P. Aufmuth, C. Aulbert, S. Babak, R. Balasubramanian, B. W. Barr, S. Berukoff, et al., Classical and Quantum Gravity **23**, S71 (2006), ISSN 0264-9381, URL http://dx.doi.org/10.1088/0264-9381/23/8/S10.

[9] Advanced LIGO Systems Group, Tech. Rep. T010075, LIGO Laboratory (2009), URL https://dcc.ligo.org/cgi-bin/DocDB/ShowDocument?docid=5489.

[10] R. Adhikari, P. Fritschel, and S. Waldman, Tech. Rep. T060156, LIGO Laboratory (2006), URL https://dcc.ligo.org/cgi-bin/DocDB/ShowDocument?docid=7384.

[11] T. Fricke, N. Smith, R. Abbott, R. Adhikari, K. Dooley, M. Evans, P. Fritschel, V. Frolov, K. Kawabe, and S. Waldman, in preparation (2011), URL https://dcc.ligo.org/cgi-bin/private/DocDB/ShowDocument?docid=8442.

[12] J. S. Kissel, Ph.D. thesis, Louisiana State University (2010).

[13] M. Frede, B. Schulz, R. Wilhelm, P. Kwee, F. Seifert, B. Willke, and D. Kracht, Opt. Express **15**, 459 (2007), URL http://dx.doi.org/10.1364/OE.15.000459.

[14] P. Willems, A. Brooks, M. Mageswaran, V. Sannibale, C. Vorvick, D. Atkinson, R. Amin, and C. Adams, *Thermal Compensation in Enhanced LIGO* (2009).

[15] H. Lück, C. Affeldt, J. Degallaix, A. Freise, H. Grote, M. Hewitson, S. Hild, J. Leong, M. Prijatelj, K. A. Strain, et al., Journal of Physics: Conference Series **228**, 012012+ (2010), ISSN 1742-6596, URL http://dx.doi.org/10.1088/1742-6596/228/1/012012.

[16] D. Garfinkle (2005), gr-qc/0511083, URL http://arxiv.org/abs/gr-qc/0511083.

[17] P. Fritschel and D. Shoemaker, Tech. Rep. T952007, LIGO Laboratory (1997).

[18] I. Group, Tech. Rep., LIGO Laboratory (1998).

[19] A. E. Siegman, *Lasers* (University Science Books, 55D Gate Five Road, Sausalito, CA 94965, 1986).

[20] D. Z. Anderson, Appl. Opt. **23**, 2944 (1984), URL http://dx.doi.org/10.1364/AO.23.002944.

BIOGRAPHICAL SKETCH

Katherine Laird Dooley was born in Rhinebeck, NY on June 10, 1984 to Janine L Protzman and Alan P Dooley. She grew up in Poughkeepsie, NY with three younger brothers and graduated from Spackenkill HS in 2002. She went to Vassar College and graduated in 2006 having focused her studies on Physics, French, and Mathematics. Kate began her Physics PhD program at the U. of Florida in the fall of 2006, and moved to Baton Rouge, LA a year later in order to carry out the entirety of her graduate research at LIGO Livingston.